NASA Technical Memorandum 110363

New Higher-Order Godunov Code for Modelling Performance of Two-Stage Light Gas Guns

D. W. Bogdanoff, Thermosciences Institute, Ames Research Center, Moffett Field, California
R. J. Miller, Ames Research Center, Moffett Field, California

September 1995

National Aeronautics and
Space Administration

Ames Research Center
Moffett Field, California 94035-1000

CONTENTS

New Higher-Order Godunov Code for Modelling Performance of Two-Stage Light Gas Guns

D. W. BOGDANOFF*

Thermosciences Institute

and

R. J. MILLER**

Ames Research Center

Summary

A new quasi-one-dimensional Godunov code for modelling two-stage light gas guns is described. The code is third-order accurate in space and second-order accurate in time. A very accurate Riemann solver is used. Friction and heat transfer to the tube wall for gases and dense media are modelled and a simple nonequilibrium turbulence model is used for gas flows. The code also models gunpowder burn in the first-stage breech. Realistic equations of state (EOS) are used for all media. The code was validated against exact solutions of Riemann's shock-tube problem, impact of dense media slabs at velocities up to 20 km/sec, flow through a supersonic convergent-divergent nozzle and burning of gunpowder in a closed bomb. Excellent validation results were obtained. The code was then used to predict the performance of two light gas guns (1.5 in. and 0.28 in.) in service at the Ames Research Center. The code predictions were compared with measured pressure histories in the powder chamber and pump tube and with measured piston and projectile velocities. Very good agreement between computational fluid dynamics (CFD) predictions and measurements was obtained. Actual powder-burn rates in the gun were found to be considerably higher (60–90 percent) than predicted by the manufacturer and the behavior of the piston upon yielding appears to differ greatly from that suggested by low-strain rate tests.

1 Introduction

In 1993, after being shut down for a number of years, the radiation ballistic range facility at the NASA Ames Research Center was reactivated. Tests were performed in 1993–94 using Ames' 0.28 in. and 1.5 in. caliber two-stage light gas guns. These tests studied, primarily, damage caused by simulated space debris impacts on space station wall segments and space shuttle tiles. Ames has long served as an agency source of expertise in light gas gun launcher research, development and testing (ref. 1). For the space debris impact tests, an increase in the gun muzzle velocity was desired to allow a more complete simulation of the possible velocity range of space debris impacts. Such a muzzle velocity increase must be accomplished with great care to avoid excessive gun erosion and the overstressing of the gun or the launch package. It would also be desirable to reduce the maximum gun and projectile base pressures and gun erosion, while maintaining muzzle velocity. Experimental gun development is very costly in time and money (there can be eight or more gun operating parameters which can be varied) and can carry considerable risk of major damage to the facility. A well-validated, user-friendly computational fluid dynamics (CFD) gun code capable of guiding the selection of gun operating parameters to safely and economically achieve increases in muzzle velocity and/or reductions in maximum gun pressures and gun erosion is needed. The code described herein has been used to help increase the muzzle velocity of the Ames 1.5 in. gun (for a fairly heavy projectile) from 6.6 to 7.1 km/sec, while, at the same time, reducing gun erosion by 50 percent.

Figure 1 shows a sketch (not to scale) of a representative two-stage light gas gun. From left to right, we see the powder chamber, the initial position of the plastic piston in the pump tube, the very long pump tube, initially filled with hydrogen or helium, the contraction section, the diaphragm just behind the projectile, the projectile in its initial position and the gun barrel (or launch tube). Upon ignition of the powder charge, the piston is accelerated to a velocity of the order of 800 m/sec. The piston travels down the pump tube, greatly compressing and heating the working gas. The working gas can be volumetrically compressed by a factor of the order of 1000, reaching pressures of roughly 10,000 bar and (theoretical) temperatures as high as 3000 K. At certain point in the

*Senior Research Scientist. NASA Ames Research Center, Moffett Field, California.

**Branch Scientist (retired), code STF.

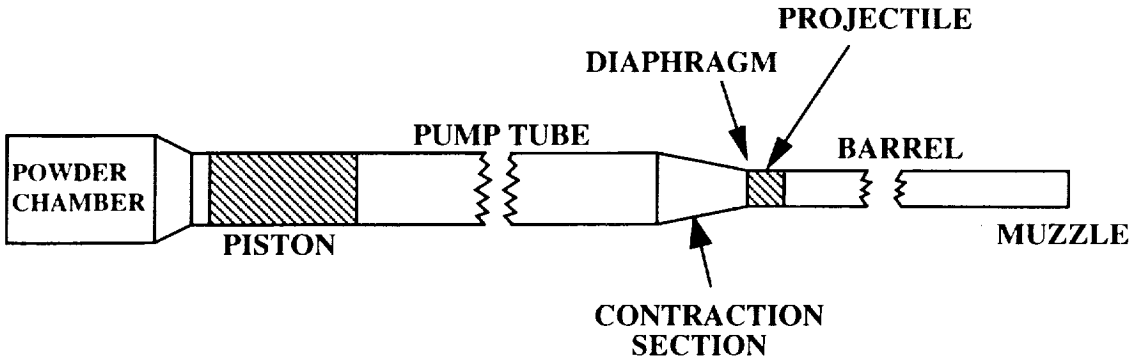

Figure 1. Representative two-stage light gas gun. Not to scale.

compression process, the diaphragm ruptures and the projectile begins to accelerate down the gun barrel.

The great advantage of the two-stage gun over a single-stage powder or gas gun is as follows. For the single-stage gun, it is difficult to obtain a sound speed of the driving gas which is much greater than 1–1.4 km/sec. This usually limits the muzzle velocity of such a gun to a maximum of 2.5–3 km/sec. With the two-stage gun technique, the energy of the powder gas is transferred, with a reasonably high efficiency, to a much smaller mass of low molecular weight working gas. The sound speed of the working gas, at maximum compression, can be as high as 4–4.5 km/sec. This permits the two-stage gun to reach muzzle velocities of 7–8 km/sec fairly routinely. With very light projectiles, and driving the gun hard, velocities as high as 10–11 km/sec can be obtained.

All media in the gun (powder/powder gas, piston, working gas, and projectile) are subject to very high pressures and temperatures and therefore should be modelled with equations of state (EOS) which are accurate under these conditions. As an example, for the gases, the ideal gas EOS is usually very inaccurate in the setting of two-stage guns. The piston and projectile may show high strain rate behavior which is very different from that which would be expected based on available low-strain rate data. Friction and heat transfer of gases and solids to the tube wall are very important, can cause reductions (refs. 2 and 3) in muzzle velocity of 10–20 percent, and should be carefully modelled. It would be desirable to assess to what extent nonequilibrium turbulence in the gas flows may affect the skin friction and heat transfer to the tube walls.

The two-stage light gas gun was not the only quasi-one-dimensional flow problem which needed to be modelled at Ames at this point in time. There was also interest in high-explosive detonations, high explosive driven ram accelerators and hypervelocity impact. These phenomena require accurate modelling at pressures from 300 kbar to 10 Mbar and higher pressures, well beyond the representative maximum pressures in light gas guns (10–15 kbar). It would be desirable to obtain a code which was capable of dealing with these very-high-pressure problems as well as for modelling light gas guns.

A number of CFD codes (refs. 3–9) for one- and two-stage guns were examined. The IBHVG2 code (ref. 5) is limited to modelling single-stage guns. The code by Charters and Sangster (ref. 3) is a two-stage gun code, but does not include friction and heat transfer and uses EOS which have limited ranges of applicability. It is known (refs. 2 and 3) that friction and heat transfer effects can cause muzzle velocity reductions of 10–20 percent. The ALE code (ref. 9) does not calculate the entire gun cycle, but rather starts with a given piston velocity history and a point mass piston. Powder-burn and piston deformation are not treated. The gas friction model does not include Mach number and wall-temperature effects. For the EOS of hydrogen, a 28-coefficient fit to tabulated data is used. The MOOREA code (refs. 7 and 8) uses a van der Waals volumetric EOS for the pump tube gas and powder gases and a segmented thermal EOS for the pump-tube gas. The latter EOS is composed of three regions, each with C_v varying as $A_iT + B_i$, where C_v is the specific heat at constant volume, T is temperature and A_i and B_i are constants, different for each region. The friction model for the piston and projectile either uses a constant force at the base of the piston or projectile or increases the mass of the piston or projectile a few percent. The LLG3 model (ref. 4) uses a volumetrically and thermally perfect EOS for the pump tube gas. The gas friction model does not include a wall-temperature effect and wall heating from piston and projectile friction do not appear to be included. The HVML89 model (ref. 6), developed from the earlier model of reference 2, uses the van der Waals EOS for the

pump-tube and powder gases and an isothermal EOS for the piston material.

None of these codes included nonequilibrium gas turbulence effects and the EOS limitations would preclude them from producing accurate results at megabar pressures. In addition, all of the code examined failed to include one or more additional phenomena which it was desired to model. The authors emphasize that there is nothing wrong with the codes discussed above when used for the purposes for which they were written and they have, in fact, yielded a large number of very useful results. Rather, they do not easily lend themselves to model all the phenomena we wished to study in two-stage light gas guns and also to study megabar pressures (at least, not without substantial modifications). Making substantial changes deep within another worker's program can be an extremely lengthy and, at times, cost-ineffective process (although one may learn to run a well-documented code written by another worker rather easily). For these reasons, taken together, it was decided to construct a new code.

The new code presented here uses the Godunov (ref. 10) technique. Briefly, the Godunov technique solves a Riemann problem at every cell boundary at every timestep in order to calculate the flux between the two cells in question at the time in question. Figure 2 shows an x-t wave diagram of such a Riemann problem. The abscissa is distance (perpendicular to the cell boundary) from one cell to the other and the ordinate is time starting from the beginning of the timestep. The initial conditions on the two sides of the cell boundary at the beginning of the timestep are conditions 1 and 4. The dynamics of the Riemann problem gives rise to a pressure wave travelling into the medium of the left cell, an interface between the two media and a pressure wave travelling into the medium of the right cell. These waves and the interface are shown in figure 2. The conditions in the two new zones 2 and 3 can be calculated to many different degrees of accuracy, as required. The flux is then calculated according to the zone in which the cell-boundary resides during the timestep in question. For the case of figure 2, if the cell boundary were motionless, its path in the x-t diagram would be vertical and it would reside in zone 2. The fluxes would then be evaluated simply and directly from the media conditions of zone 2. The technique is exceedingly flexible. No assumptions about the EOS of the media are necessary. It is not necessary to explicitly insert any artificial viscosity. Extrapolations (or interpolations) to the cell boundary in question can be first, second, third, or even higher order accuracy. The Riemann solver can be first, second, or higher order accurate and its order of accuracy can readily be changed to suit the problem in question.

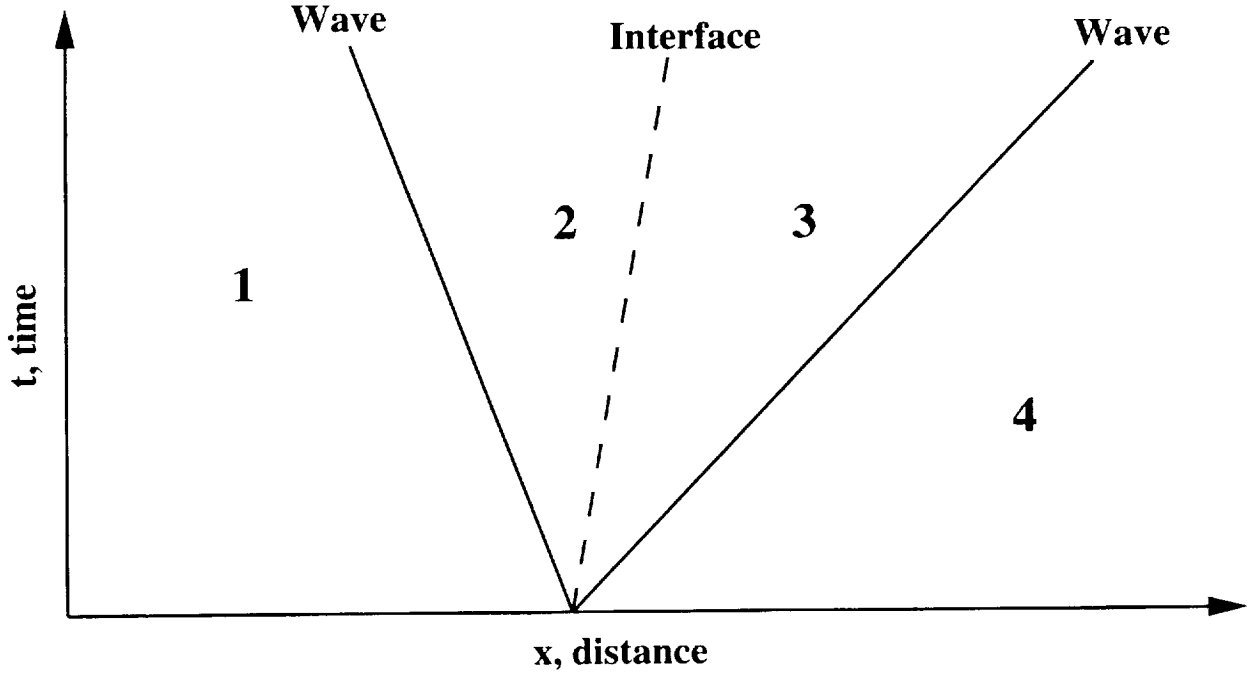

Figure 2. x-t wave diagram for Riemann problem between two cells. Initial conditions at beginning of timestep are those in regions 1 and 4. Waves progress into both these regions and an interface separates the media initially in regions 1 and 4.

The features of the new higher-order Godunov code presented herein include the following:

(1) It models the complete two-stage gun cycle, from the start of powder burn, to the projectile exiting the muzzle.

(2) It uses the Godunov technique, outlined above, which has been shown (ref. 10) to be very robust for dense media and extremely high velocities. It is third order accurate in space and second-order accurate in time. The Riemann solver used is of very high accuracy, being exact for shocks and using a very accurate power law integration scheme for expansion waves.

(3) It uses realistic EOS for all media. The EOS for solids includes the effects of both density and energy on pressure and would remain valid for megabar pressures. Simple models for high strain rate effects can be introduced into the modelling of the piston and the projectile.

(4) Friction and heat transfer from gases and dense media to the tube wall are included. The gas-phase friction and heat-transfer model includes compressibility and wall-temperature effects. A simple model for nonequilibrium gas turbulence is included.

(5) The basic algorithms are capable of producing accurate results at pressures well into the megabar range. Thus, the code could be used to model high explosive detonations or hypervelocity impact phenomena. During the validation of the present code using exact analytical solutions (see sec. 4.2), accurate CFD solutions were obtained at pressures up to 8 megabars. A earlier version of the code (ref. 10) has produced accurate solutions at pressures up to 10,000 megabars.

(6) The code is well-documented and user-friendly versions exist for Cray and HP computers. The documentation includes descriptions of all the physics modelled, the algorithms used and approximations made. A manual is available, giving complete instructions for the use of the code.

This technical memorandum will discuss all aspects of the higher-order Godunov code. The governing equations, source terms and boundary conditions (bc) will be discussed along with the accompanying numerical methods. The code will be validated, in part, by comparison with a number of exact analytical solutions. Further validation will be shown by comparison with recent, extensive experimental data from Ames' 0.28 in. and 1.5 in. caliber light gas guns. The code has been found to be very useful in a theoretical and experimental study (ref. 11) of the technique of inserting an extra diaphragm into the pump tube of a two-stage gun in order to increase gun performance. The code has been used to guide modifications of the operating conditions of the Ames 1.5 in. gun to yield muzzle velocity increases (for a moderately heavy projectile) from 6.6 to 7.1 km/sec and, at the same time, a 50 percent decrease in gun erosion (ref. 12). Further, it has yielded some very interesting insights into the burning of gunpowder in the first-stage breech and the apparently anomalous yielding behavior of the pump tube piston. These last two results will be presented herein.

Support for DWB by NASA (Contract NAS-2-14031) to Eloret is gratefully acknowledged.

2 Formulation

In this section, we present the formulation of the problem. The governing gasdynamic equations are presented in section 2.1. The various options available for the EOS of the media are presented in section 2.2. Sections 2.3–2.6 present the formulation of the various source terms which appear in the equations. These include the wall-pressure term, friction and heat-transfer terms for gases and dense media and the gunpowder combustion terms.

2.1. Governing Equations

The quasi-one-dimensional gasdynamic equations used, written in conservation form, are

$$A\frac{\partial U}{\partial t} = -\frac{\partial (FA)}{\partial x} + H\frac{\partial A}{\partial x} + AW + \pi DV \qquad (1)$$

where the state vector is given by

$$U = (\rho, \rho u, e_t, \rho m_1, \rho m_2, \ldots) \qquad (2)$$

the flux vector is given by

$$F = (\rho u, \rho u^2 + p, u(e_t + p), \rho u m_1, \rho u m_2, \ldots) \qquad (3)$$

the wall-pressure component of the source term is given by

$$H = (0, p, 0, 0, 0, \ldots) \qquad (4)$$

the chemical-reaction component of the source term is given by

$$W = (0,0,0,w_1,w_2,\ldots) \tag{5}$$

and the wall-friction and heat-transfer component of the source term is given by

$$V = (0,\tau,q,0,0,\ldots) \tag{6}$$

where A denotes cross-sectional area, D, tube diameter, ρ, density, u, velocity, e, the internal energy per unit mass, p, pressure, m_i, mass fraction of the ith component, $e_t = \rho(e + u^2/2)$, w_i, the species mass generation rate per unit volume for the ith component, $-\tau$, the wall-shear stress and $-q$, the wall-heat flux. The speed of sound, c, temperature and pressure are obtained from the EOS described below. The code uses a finite volume formulation with state variables calculated at the center of each computational cell.

2.2 EOS

The code offers a number of EOS options. We will describe them below. (The label numbers given refer to those used in our CFD code.) Option #1 uses the Abel (ref. 13) volumetric EOS,

$$p(v-b) = \frac{R_u T}{m} \tag{7}$$

where p is pressure, v, specific volume, b, molecular volume, R_u, the universal gas constant, T, temperature and m, molecular weight. The enthalpy is determined assuming constant specific heat. This option can be used with single or multiple species. Option number #2 also uses equation (7), but determines the enthalpy with variable specific heats using data from the Joint Army-Navy-NASA-Air Force (JANNAF) tables (ref. 14). Again, this option can be used with single or multiple species. Option #3 is Zel'dovich and Raizer's three term dense media EOS (ref. 15) with the third term neglected. This term was dropped because:

(1) it is an electron temperature term which is very small for the dense media conditions of interest here,

(2) calculation of shock Hugoniots for the piston and projectile material using two terms only of the Zel'dovich and Raizer EOS shows excellent agreement with the experimental data of reference 10 up to megabar pressures, and

(3) its inclusion significantly complicates the solution of the EOS in the code and slows down the code appreciably.

From the experimental shock Hugoniot data of reference 16 for a given medium, a good determination of the constants in this EOS can be made. Option #4 is a two-dimensional tabulated EOS of the form $T(\rho,e)$, $p(\rho,e)$. From the tabulated grid-point values, bi-cubic interpolations are made in logarithmic space to obtain values of T, p, $p_{\rho,e}$, and $p_{e,\rho}$ at the desired point. The sound speed is then calculated from p, ρ, $p_{\rho,e}$, and $p_{e,\rho}$. For the hydrogen gas used in the current CFD code, the EOS was constructed as follows. First, equilibrium calculations were made for point hydrogen molecules (and atoms) over the full required pressure and temperature ranges. Then, a molecular volume term was added which follows the Zel'dovich and Raizer (ref. 15) cold pressure-volume relation for dense media.

$$p = A\left[\left(\frac{\rho}{\rho_o}\right)^n - 1\right] \tag{8}$$

where ρ_o is a reference density and A and n are empirical constants for the medium in question. The constants in equation (8) for hydrogen were determined by fitting the experimental shock Hugoniot data (ref. 16) for liquid hydrogen to the Zel'dovich and Raizer's three term dense media EOS (ref. 15) with the third term neglected. It can be shown that this yields an EOS for hydrogen which compares rather well with the tabulated SESAME (ref. 17) EOS. There are about twice as many grid points per decade in our gridding than for the SESAME EOS, which was designed for an extremely wide range of densities and temperatures, i.e., densities from 5×10^{-6} to 1750 gm/cm^3 (for hydrogen) and temperatures from 0.04 to 30,000 electron volts. The higher density of grid points considerably improves the accuracy and smoothness of interpolated results.

Two options are available for two-phase EOSs for the gunpowder/powder gas regions. Option #7 uses the tabulated EOS for the gas phase and a simple model with constant density and internal energy for the solid phase. Option #8 uses the option #1 (with one species only) for the gas phase and the constant density, constant internal energy model for the solid phase. In the gun solutions presented herein, option #8 was used for the

gunpowder/powder gas regions, option #4 for the piston and projectile and option #6 for the hydrogen gas.

2.3 Source Terms–Wall-Pressure Term

When there is an area change over the length of a computational cell, a momentum source term is required in the equations. A simple way to evaluate this term would be as follows.

$$F_w = \frac{p_l + p_r}{2} \Delta A \qquad (9)$$

where F_w is the wall-pressure force (source) term, ΔA is the area change and p_l and p_r are the pressures at the left and right ends of the cell. The average pressure acting over the wall is assumed to be $(p_l + p_r)/2$. A more sophisticated technique can be used to evaluate F_w, as follows. Parabolic fits are made to the channel area profile and the pressure variation along the channel. These can then be integrated over the cell length to provide a more accurate estimate of F_w. In code proof tests in a supersonic convergent-divergent nozzle, the more sophisticated evaluation of F_w yielded significantly lower errors and, hence, has become a permanent part of the code.

2.4 Source Terms–Gas-Phase Friction and Heat-Transfer Terms

The calculation of these terms is presented in some detail in Appendix A and, hence, will only briefly be outlined here. We start with the well known (refs. 18 and 19) skin friction correlations for pipe flow. We base a correction for the effects of Mach number and the difference between the wall temperature and the average stream temperature on the correlations developed by van Driest (ref. 20). We have developed a "reference temperature" technique which fairly accurately reproduces the variations of skin friction coefficient, f, with Mach number and the (wall temperature)/(stream temperature) ratio given by van Driest's correlations. The turbulent component of f is then corrected for nonequilibrium turbulence effects as described in Appendix B and briefly, in the next paragraph. With f determined, the wall friction momentum term follows directly. We then use a form of Reynolds' analogy (ref. 21) to estimate the wall-heat transfer energy term. For regions with gas and solids (gunpowder/powder gas), the wall friction and heat-transfer terms are based on the gas properties only. This two-phase flow condition applies only in the upstream part of the pump tube for the first part of the solution before all the powder is burned. Currently, T_w is prescribed and held fixed at 300 K. At a later time, the code will be modified to allow for wall-heating effects.

A simple model (App. B) was developed which assumes that the nonequilibrium turbulence kinetic energy (TKE) relaxes towards the equilibrium value for the flow in question with an e-folding length which is a certain number of tube diameters. (The e-folding length is the distance along the tube over which the difference between the nonequilibrium and equilibrium TKE would drop to 1/eth of its original value in a steady flow with constant cross-section.) The range of Reynolds numbers (Re) for hydrogen flow in the pump tube is typically 3×10^5 to 3×10^7. Detailed turbulence measurements (refs. 22 and 23) for fully developed pipe flow were found at a maximum Re of 5×10^5. This Re is within our range, but towards the low end of it. However, turbulent pipe flow does not appear to change very rapidly with Re over the Re range of interest (at least over the range 3×10^5 to 3×10^6 reported in ref. 24). Hence, a rough estimate of the number of pipe diameters required for relaxation of the turbulent kinetic energy towards the equilibrium value was obtained from the data of references 22 and 23. This number (3.27 diameters) was used in our model. By writing a simple TKE equation with this relaxation term and the appropriate convection terms across cell boundaries, the TKE in any cell at any time can be calculated. With values for the nonequilibrium and equilibrium TKEs in hand, the turbulent portion of the skin friction coefficient is multiplied by a term $(TKE_{nonequil}/TKE_{equil})^{0.5}$, to reflect the increased transport of momentum and energy due to nonequilibrium turbulence. Further details are given in Appendix B.

2.5 Source Terms–Solid-Phase Friction and Heat-Transfer Terms

The calculation of these terms is also presented in some detail in Appendix C and will only briefly be outlined here. Our technique is a variation of that presented in reference 4. First, the normal stress on the tube walls is calculated from the axial pressure which appears in the CFD code using a simple elastic-plastic model. This stress is first calculated, assuming elastic behavior, taking into account (1) the initial jamming of the solid into the tube and (2) the axial (CFD) pressure term. For the piston, the initial jamming is produced by cooling the piston in a freezer (which causes it to contract), inserting it into the pump tube and allowing it to return to room temperature. As the piston temperature rises, it expands and generates jamming stresses. If the calculated difference between the axial and normal stresses is found to be greater than the yield stress, this difference is simply set to the yield stress. This latter procedure is the plastic part of the modelling.

The friction coefficient between the solid and the walls, as a function of velocity, is modelled from the experimental data of reference 25, following the techniques of references 26–28. The friction force on the wall is then calculated and limited by the estimated shear yield stress of the solid, following reference 29. The momentum source term follows directly. The energy source term is simply taken to be 1/2 × (friction source term) × (velocity). This term is a loss of energy from the solid to the wall due to frictional heating. The other half of the heat generated by the frictional work is assumed to flow to the solid and therefore does not represent an energy loss from the solid.

2.6 Source Terms–Gunpowder Burn

The powder grains are of the standard form of circular cylinders with a number (usually 0, 1, or 7) of circular perforations parallel to the outer cylinder axis. The linear surface regression rate, r, of the powder is taken to follow the usual ballistics expression (see, for example, ref. 30)

$$r = ap^n \tag{10}$$

where p is the pressure and a and n are constants given by the maker of the powder or by military testing laboratories. The specific energy released upon burning of the gunpowder, ΔE, is calculated from

$$\Delta E = E(\text{powder gas}) - E(\text{solid powder}) \tag{11}$$

$$E(\text{powder gas}) = \frac{I}{\gamma - 1} \tag{12}$$

$$I = \text{Impetus} = \frac{R_u T_A}{M} \tag{13}$$

where E(solid powder) is the internal energy of the solid powder, γ is the specific-heat ratio of the powder gas, R_u is the universal gas constant, T_A is the adiabatic flame temperature of the powder and M is the mean molecular weight of the powder gas. I (the "impetus"), γ, and M are given by the powder manufacturer. E(solid powder) is estimated at room temperature from the specific heat of the powder. The density and energy of the unburned powder are assumed to remain constant at their room temperature values. Thus, no heat transfer to the powder is considered.

With the initial shape of the powder grains known, the linear regression rate calculated using equation (10) and the specific energy release of the powder upon combustion known, the necessary powder burn source terms for energy deposition and change of powder into powder gas can readily be evaluated. The amount of powder burned per cell per timestep is calculated using a predictor-corrector method, so it is second-order accurate in time.

The unburned powder and the powder gas are assumed to move together—there is no relative motion between the two phases and, hence, no erosive burning effects due to relative gas-powder velocity differences. The powder is also assumed to be distributed at a uniform density throughout the first-stage breech. This avoids the production of spurious slosh wave effects. These were deliberately accepted limitations made to allow the code effort to concentrate on two-stage effects, that is, piston, hydrogen, and projectile dynamics. The code thus is not suitable for the detailed study of single-stage military-type weapons where relative motion between the gas and the powder and erosive burning effects can be important. From the comparison between experimental and theoretical powder-chamber and pump-tube pressure histories and piston velocities (see secs. 5.3 and 5.4), the above assumption will prove to be very good for the present purposes.

3 Numerical Method

The numerical method will be described in this section. The method of updating of the cell-center state variables in time is presented in section 3.1. The extrapolations, interpolations and limiters used to calculate the primitive variables at the cell boundaries are described in section 3.2. The Riemann solvers used to calculate the fluxes at the cell boundaries are presented in section 3.3. Calculations of the conditions at the zone boundaries are described in section 3.4. The multiple zoning techniques used, including the selection of the distributions of cell sizes in the various zones, are described in section 3.5. Finally, the techniques used to model jamming or bouncing of the pump-tube piston are presented in section 3.6.

3.1. Code Advancement in Time

To calculate the fluid dynamic part of the time step, the code employs an explicit MacCormack predictor-corrector differencing scheme (ref. 31) which is second-order accurate in time. For this purpose, the solution to equation (1) is advanced in time for the predictor and corrector as follows.

$$U^{\overline{n+1}} V^{\overline{n+1}} = U^n V^n + \left[\left(F_L^n A_L^n - F_R^n A_R^n \right) + F_S^n \right] \Delta t \tag{14}$$

$$F_S^n = \left(0, \bar{p}\Delta A + \tau A_w, qA_w, 0, 0, \ldots.\right)^n \quad (15)$$

$$U^{n+1}V^{n+1} = U^nV^n + \left[\left(F_L^{n'}A_L^{n'} - F_R^{n'}A_R^{n'}\right) + F_S^{n'}\right]\Delta t \quad (16)$$

$$F_S^{n'} = \left(0, \bar{p}\Delta A + \tau A_w, qA_w, 0, 0, \ldots.\right)^{n'} \quad (17)$$

$$F^{n'} = \frac{F^n + F^{\overline{n+1}}}{2} \quad (18)$$

where

U = state vector

V = cell volume

A_L, A_R = left- and right-cell boundary areas

ΔA = $A_R - A_L$

A_w = projection of cell wall area normal to axis

F_L, F_R = left- and right-cell boundary fluxes

F_S = fluid dynamic source term

Δt = time step

q = wall heat flux

τ = wall shear stress

$\bar{p}$ = "average" cell pressure

n superscript denotes conditions at start of step

$\overline{n+1}$ superscript denotes conditions at end of predictor step

n+1 superscript denotes conditions at end of corrector step

n' superscript denotes average of the fluxes evaluated at the n and $\overline{n+1}$ time levels

For details of the calculations of the $\bar{p}\Delta A$, τA_w, and qA_w terms, see sections 2.3–2.5 and Appendices A–C. When the computational grid slides, $V^n \neq V^{\overline{n+1}} \neq V^{n+1}$ and the areas must be carefully averaged values. Otherwise, spurious source terms can be generated. If the cell center e or ρ values calculated from equations (14) and (16) are less than a given fraction (f_{cr}) of the value at the beginning of the timestep, they are reset to that fraction. The best performance was found when f_{cr} was in the range 0.3–0.5. The results presented herein were calculated with f_{cr} equal to 0.5. This safety device is invoked only very rarely, when very strong shock waves are involved.

After the above second-order fluid dynamic advancement in time is performed, a second-order time accurate "chemistry in a closed box" powder-burn calculation is made, as described in section 2.6. For the powder burn, the solution to equation (1) is advanced in time for the predictor and corrector as follows.

$$U^{\overline{n+1}}V^n = U^nV^n + F_{sb}^n\Delta t \quad (19)$$

$$F_{sb}^n = V^n\left(0, 0, w\Delta E_b, -w, w\right)^n \quad (20)$$

$$U^{n+1}V^n = U^nV^n + F_{sb}^{n'}\Delta t \quad (21)$$

$$F_{sb}^{n'} = V^n\left(0, 0, w\Delta E_b, -w, w\right)^{n'} \quad (22)$$

where

F_{sb} = powder burn source term

w = mass of powder consumed per unit volume, per time

ΔE_b = energy released upon powder burn, per unit mass of powder

In the formulation of equations (19)–(22), only two species are considered, unburned gunpowder and powder gas. Also, since the chemistry takes placed in a fixed, closed box, the volume, V^n, is the same at all time levels; it is included in equations (19)–(22) simply to place them in the same form as equations (14)–(18). Since these two second-order procedures are completely separated in the time step, the interaction between them is only first-order accurate in time. For the current purposes of gunpowder burn only, this does not cause any difficulties. Since the method is explicit, the von Neumann stability criterion (ref. 32) that the CFL number be less than one must be applied. Most of our results were obtained at a CFL number of 0.7.

3.2 Determination of Cell Boundary Values

The fluxes at the cell boundaries are calculated from values of the primitive variables (ρ, u, e, and m_i) on the two

sides of the cell boundary. The cell-boundary values are obtained from extrapolation or interpolations of the cell-center values. All extrapolations and interpolations are made by cell numbers, taking no account of the physical sizes of the cells. Most of the calculations of internal cell-boundary values are with third order extrapolations and interpolations. Six sets of variables with which to extrapolate and interpolate were tested before deciding on (ρ, u, e, and m_i). In these six sets of variables, the second variable was either u or ρu and the third variable was either e, ρe, or e_t. In extensive testing with the Reimann shock tube problem at a pressure ratio of 1000, the primitive variables gave the best combination of minimum oscillation size (about 1–2 percent) and minimum spurious entropy production and heating. (Small, rapidly damped oscillations of amplitudes of 1–2 percent sometimes appear in the solutions in the neighborhood of strong shock waves.)

Figure 3 illustrates the extrapolation and interpolation procedures. We consider the right-side boundary value of a primitive variable at the boundary 1–2 between cells 1 and 2. The cell-center values are indicated by the dots for cells 1 to 4. At the boundary 1–2, third-order extrapolation gives the value 3e, third-order interpolation gives the value 3i and second-order extrapolation gives the value 2, all indicated by open circles. The choice of boundary values used in the present code is as follows. If the 3i value is between the 3e and 2 values, it is used as the final extrapolation/interpolation value. If the interpolated value is outside the range of the 3e and 2 values, whichever of the 3e and 2 values is closest to the 3i value is taken as the final extrapolation/interpolation value. So, for the case shown in figure 3, the 3e value would be selected.

For the cell boundary one cell removed from a zone boundary, extrapolation/interpolation from the zone boundary towards the cell boundary is generally of second order only. This is because only one, rather than two, ghost cell is used beyond each zone boundary. The reason for dropping to second order at this location is that when constructing ghost cells across a boundary between two very different media, there is a considerable degree of freedom even in constructing a single ghost cell. We were

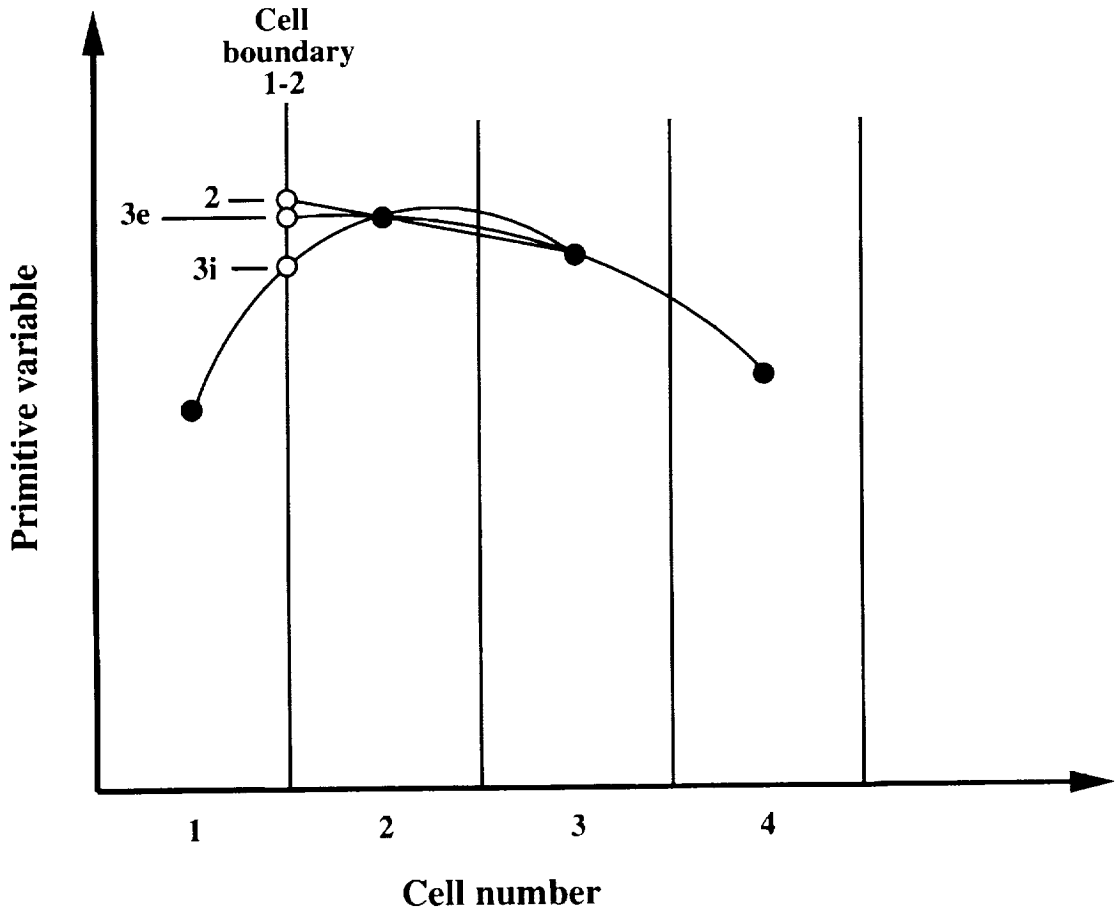

Figure 3. Illustration of extrapolation and interpolation from cell-center to cell-boundary values.

able to find reasonable, robust solutions for this problem with single ghost cells. However, for two ghost cells, the degree of freedom becomes much more severe, and it was judged better not to broach the problem, but rather to remain with a single ghost cell.

In addition, for some simple inlet and outlet conditions, such as constant condition inlet or constant pressure outlet, simple first-order bc were used at the inlet or outlet zone boundaries. These first-order conditions were used only for proofing of the code and were not used for any gun solutions presented herein. All of the gun solutions presented herein used third-order extrapolations/interpolations, except as described in the preceding paragraph. The code has, however, options to be run with second- or first-order extrapolations and has occasionally been so run, when problems occurred during the initial code development and debugging.

After the extrapolations/interpolations of the primitive variables have been done to the cell boundaries, they are limited to prevent them from being outside the range of the cell-center values straddling the cell boundary in question. This procedure is illustrated in figure 4. The abscissa is the original extrapolated/interpolated value and the ordinate is the final limited value. The diagonal line through the origin is at a 1:1 slope. The solid line represents the limited primitive variable. Basically, the limited value is taken to be the extrapolated/interpolated value if it is between the cell-center values, but if it is outside the range of the cell-center values, the nearest cell-center value is substituted instead. A refinement has been added, however, as shown in figure 4. Instead of using abrupt breaks at the change points between the use of full extrapolated/interpolated values and the use of cell-center values, we have found superior code results to be obtained if one uses parabolic blending in these regions, as shown in figure 4. The size of the parabolic blending regions is much exaggerated in figure 4 (by about a factor of 6) for clarity. A value of δ/L of 0.025 was found to work well.

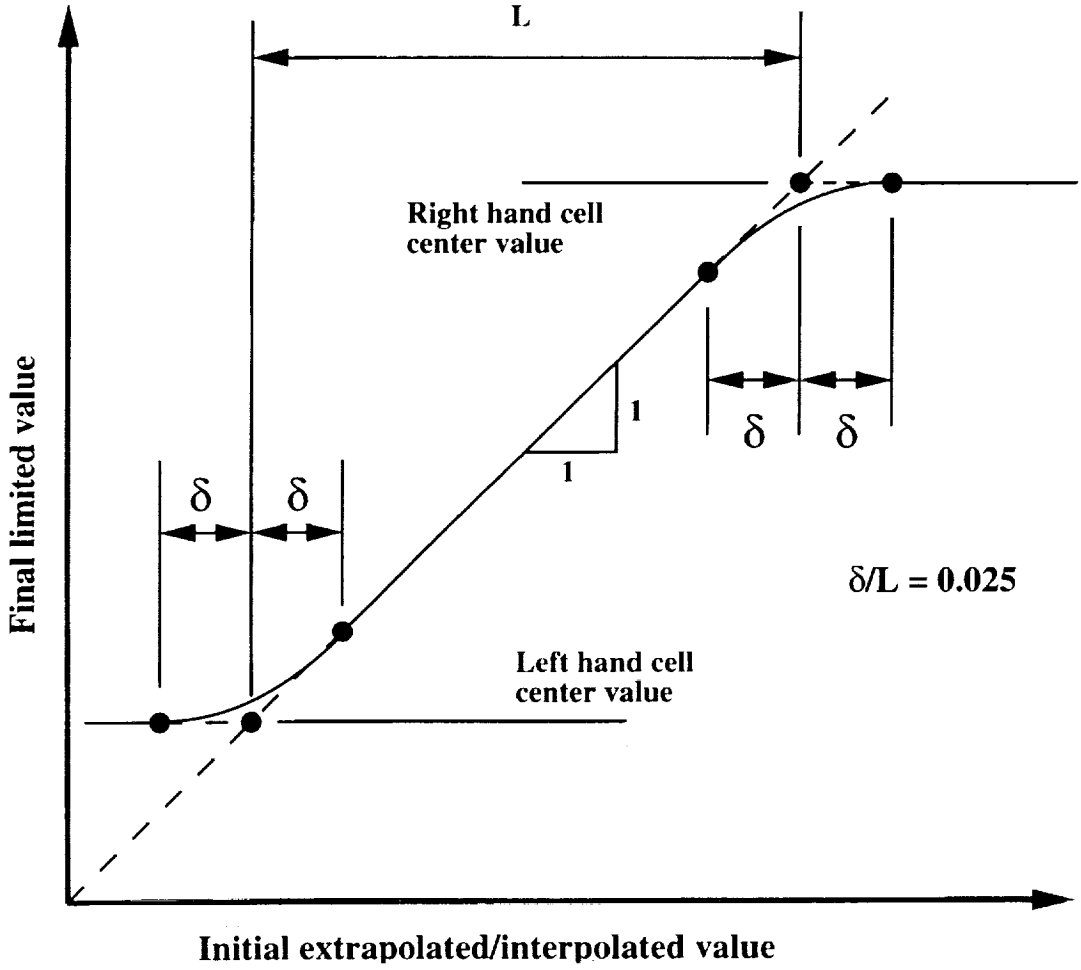

Figure 4. Illustration of parabolic blending of the limiting of extrapolated/interpolated cell-boundary values.

The above limiting processes were found to be insufficient for calculations of very strong waves. A "strong wave limiting" (SWL) process, described below, was found to be necessary. Consider the extrapolation/interpolation procedures from the right hand direction to obtain the cell-boundary conditions between cells 1 and 2 in figure 1. Across each of the cell boundaries involved in the extrapolation/interpolation procedures, i.e., boundaries 1–2, 2–3, and 3–4, we assess the strength of the waves present by calculating the following three parameters, $\beta 1$, $\beta 2$, and $\beta 3$. We then find the largest

$$\beta_1 = \frac{|u_l - u_r|}{\min(c_l, c_r)} \tag{23}$$

$$\beta_2 = \frac{|p_l - p_r|}{\min(\rho_l c_l^2, \rho_r c_r^2)} \tag{24}$$

$$\beta_3 = \frac{|\rho_l c_l - \rho_r c_r|}{\min(\rho_l c_l, \rho_r c_r)} \tag{25}$$

of the nine β values (three types of β values, each at three different cell-boundary locations) and denote it by β_{max}. (In eqs. (23)–(25), c denotes the sound speed and the subscripts l and r denote conditions on the left- and right-hand sides of the boundary.) We use this β_{max} value to decide if strong waves are present in the extrapolation/interpolation zone and hence, whether further limiting towards first-order values is required. If β_{max} is greater than a critical value, α_1, the extrapolated value is replaced the corresponding first-order cell-center value. If β_{max} is less than a second critical value, α_2, the higher-order extrapolated/interpolated value is used without further modification. If β_{max} is between α_1 and α_2, a linear blend of first- and higher-order values is used. This linear blend assures that there is always a smooth, progressive change from higher order to first order as the wave becomes stronger. The values for α_1 and α_2 used in the current code are 8 and 4. By referring to equations (23)–(25), one may see that this means that the SWL limiting process is only used in a very few places in the code where extremely strong waves are present. We note here that if the extrapolation/interpolations are second order rather than third order, the β values of equations (23)–(25) would be examined at only two cell boundaries, instead of the three as in the above discussion. The extrapolation/interpolation and limiting procedures are essentially the same at zone boundaries as at cell boundaries as described above.

3.3 Flux Calculations

With the left- and right-side values of the primitive variables at the cell or zone boundary determined as described above, the fluxes across the boundary are determined using a Riemann solver, as for any Godunov-type method. Figure 5 shows typical Riemann solutions. Zones 1 and 4 in each case are the left- and right-side conditions, extrapolated/interpolated as described above. In figure 5(a) is shown the usual Riemann solution, with two waves, in this case an expansion wave (E) and a shock wave (S) and an interface. Two new regions, 2 and 3, are created by the Riemann solution dynamics.

Depending upon the initial conditions in zones 1 and 4, the two waves can be expansion and shock (E,S) (as shown in fig. 5(a)) or (S,E), (S,S), or (E,E). If two very powerful expansions are created in the Riemann problem, it may be necessary to include a fifth, minimum pressure, zone as shown in figure 5(b). This would be a vacuum region for a situation where at least one of the regions 1 and 4 was a gas or a region at the tensile yield stress if both regions 1 and 4 were dense media. Our code does not have the ability to model spall, that is, to create new free surfaces in solids under high-tensile stresses. Rather, the solid is modelled as capable of stretching indefinitely at the yield stress. While this obviously makes the code unsuited for modelling spall situations, both CFD work and experimental observations of conditions of the piston and projectile in light gas guns strongly suggest that this code limitation is of little consequence for almost all light gas gun operating conditions modelled. The solutions obtained can, of course, be monitored for the occurrence of stresses at the tensile yield level in solid material zones.

The essential components of the Riemann solver are expansion and shock solvers. The differential form for a general isentropic expansion or compression is given in equations (26)–(28) below.

$$dp = c^2 d\rho \tag{26}$$

$$de = \frac{p}{\rho^2} d\rho \tag{27}$$

$$du = \pm \frac{dp}{\rho c} \tag{28}$$

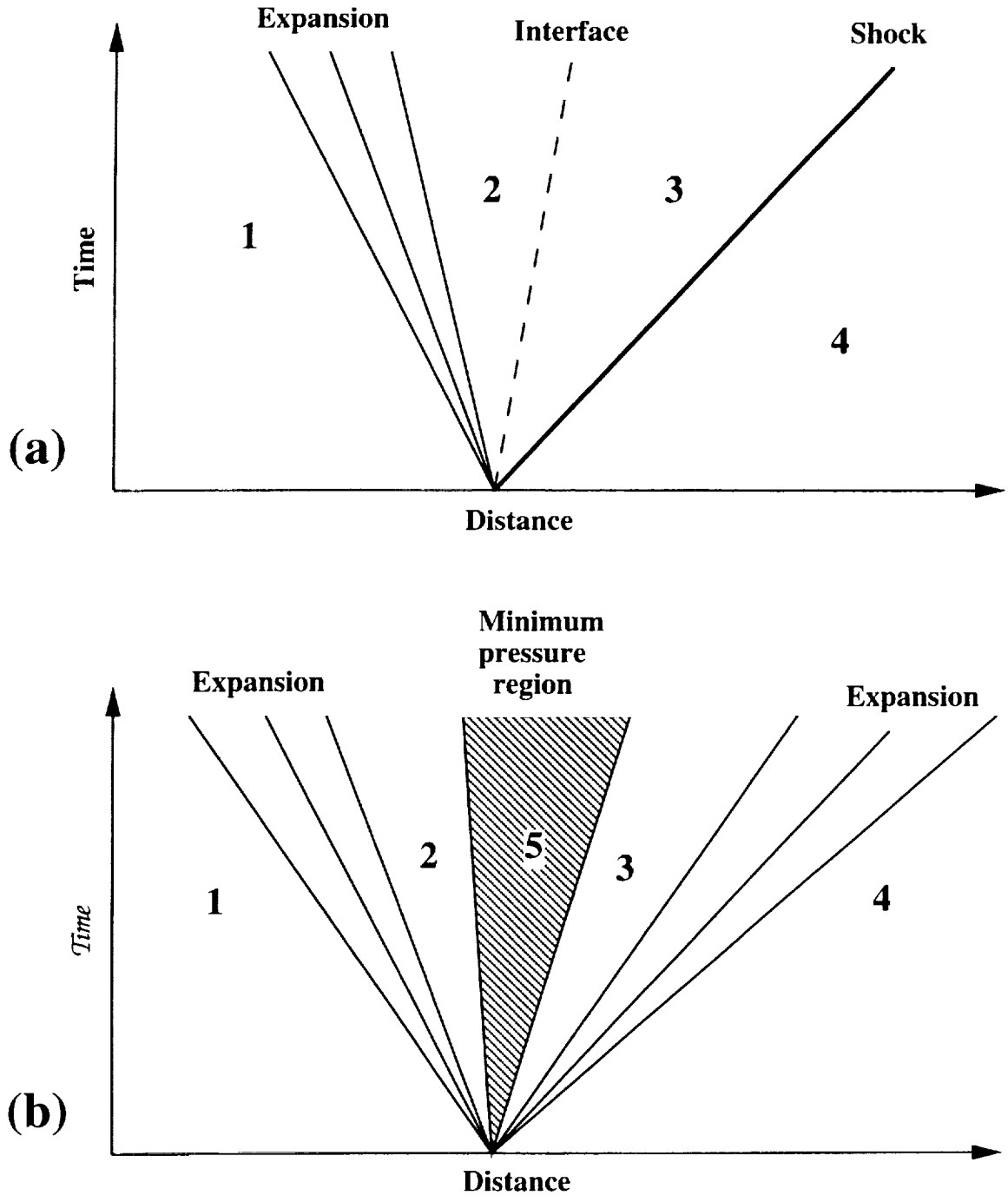

Figure 5. Riemann problems at cell or zone boundary. (a) Shows the usual problem, with two waves and an interface; (b) shows the special problem, with two very strong expansions and a minimum pressure or vacuum region between the expansions.

For a weak wave (either expansion or compression), with |du/c| not more than 0.03, the above expressions are used in the code with little modifications. For stronger waves, more accurate expressions are required.

The calculation of stronger expansion waves starts with the determination of the exponent relating the sound speed variation with the density variation, i.e., α in equation (29) below.

$$\frac{c}{c_1} = \left(\frac{\rho}{\rho_1}\right)^{\alpha} \tag{29}$$

This is determined by varying the density a small amount from the starting condition. (The starting condition is denoted by subscript 1 in eq. (29)). It turns out that this exponent is, in fact, very nearly constant for a wide range of real media even for very deep expansions. Hence, with α determined for small density variations and then assumed constant for substantial density variations, rather good exact integrations of equations (26)–(28) can be obtained. These can be readily derived and hence, are not given here. These integrations were used for expansions in our Riemann solvers. The integrations can easily be carried out to either a specified velocity or pressure. The calculated values of the density and energy at the end of the expansion are limited, in that they are not allowed to go below 1 percent of the corresponding initial values. Such limiting need be applied only for a very small number of cases in a typical solution.

Three shock wave solvers have been used with success in the code. The first is a linear solver with density limiting; equations (30)–(34) are used in this case.

$$p_2 = p_1 + \rho_1 c_1 |u_2 - u_1| \tag{30}$$

$$\rho_2 = \rho_1 + \frac{p_2 - p_1}{c_1^2} \tag{31}$$

$$\rho_{LIM} = r_\rho \rho_1 \tag{32}$$

$$\rho_{2f} = \min(\rho_2, \rho_{LIM}) \tag{33}$$

$$e_2 = e_1 + \frac{1}{2}(p_1 + p_2)\left(\frac{1}{\rho_1} - \frac{1}{\rho_{2f}}\right) \tag{34}$$

The conditions with subscripts 1 and 2 are before and after the shock, respectively. Equations (30) and (31) are derived directly from equations (26) and (28) above. Since the density ratio is known to be limited for strong shocks, the derived value of ρ_2 is limited to ρ_{2f} using equations (32) and (33). The values of r_ρ are constants for each media input into the CFD code. Reasonable values are selected after considerable study of the behavior of each media. For gunpowder/gunpowder gas, polyethylene and hydrogen, the values of ρ_r chosen were 9.55, 2.2, and 9.0, respectively. Equation (34) for the energy, e_2, is exact if the values of p_2 and ρ_{2f} were exact.

The second solver, a quadratic solver, is presented next. This solver was derived independently (ref. 10) by one of the authors (DWB), but afterwards was found to also be used by workers at Los Alamos (ref. 33). The pressure

$$A = \frac{r_\rho}{r_\rho - 1} \tag{35}$$

$$p_2 = p_1 + \rho_1 c_1 |u_2 - u_1| + A\rho_1 (u_2 - u_1)^2 \tag{36}$$

$$\psi = \frac{|u_2 - u_1|}{c_1} \tag{37}$$

$$\rho_2 = \frac{\rho_1}{1 - \frac{\psi}{1 + A\psi}} \tag{38}$$

velocity relation of the linear solver, equation (30) is modified with the addition of a quadratic term in the velocity difference to yield equation (36). With the pressure and velocity behind the shock known, the continuity and momentum equations can then be used to obtain the density behind the shock; the result is given in equations (37) and (38). The energy behind the shock is obtained from equation (34), as was done for the linear solver.

The third solver option is our "exact" shock solver, which iterates to obtain the post-shock conditions. Using the "exact" solver option, when ψ is less than 0.03, the code defaults to the linear solver. The "exact" solver guesses ρ_2, limited by the values ρ_1 and $r_\rho \rho_1$ and uses the continuity, momentum, and energy equations to calculate p_2, u_2, and e_2. The EOS is then used to generate $p'_2(\rho_2, e_2)$. ρ_2 is then iterated until p_2 equals p'_2. The iteration is

stopped when the number of iterations reaches 12 or the normalized p_2 error reaches 0.005, whichever occurs first. Essentially no improvement was found during code development by increasing the number of iterations to 24 and decreasing the acceptable p_2 error to 0.001. Thus, the accuracy given here is believed to be quite sufficient for a shock wave solver used within a Riemann solver.

A set of code development checkout runs were made with the impact of two polyethylene slabs at a closing velocity of 20 km/sec. One of the slabs is backed by an infinitely stiff plate. The outside surface of the other slab is free. Thus, the problem produces two initial shock waves, one reflected shock wave and a reflected expansion wave. Exact solutions can readily be calculated for this problem up to a certain point in time. A large improvement in the solutions was noticed when shifting from the linear to the quadratic shock solvers described above. A smaller, but still noticeable improvement in the solution was noticed when shifting from the quadratic to the "exact" shock solver. Hence, in the solutions presented herein, the "exact" shock solver was always used. There is a penalty in CPU time in shifting towards the better shock solvers. For the slab impact code checkout runs, the run times were found to be essentially in the ratio 1:2:4 for use of the linear, quadratic, and "exact" shock solvers, respectively.

We now move on to the method used to obtain a complete Riemann solution, with all 4 (or 5) zones shown in figure 5. First, complete expansion waves are calculated from the two initial zones 1 and 4 to see if the situation with the minimum pressure zone of figure 5(b) exists. If it does, then, at that point, the complete solution with all waves and regions has already been found. In the vast majority of cases, the minimum pressure zone is not required and we have the situation shown in figure 5(a) with four zones (though not, of course, necessarily with the particular pair of waves—expansion/shock—shown in the figure). The following procedure is then used to solve the problem. Two linear (acoustic) p-u equations (similar to eq. (30)) are written across the two waves between regions 1 and 2 and also between regions 3 and 4. These two equations are solved by setting $u_2 = u_3$ and $p_2 = p_3$ to yield a value for $u_2 = u_3$. (The $p_2 = p_3$ values are discarded.) Then, the higher-order expansion and shock solvers discussed above are used from u_1 to u_2 and also from u_4 to u_3 to generate new values for p_2 and p_3, which do not, in general, agree with each other initially. The key to our procedure is the technique of selecting the updated value of $u_2 = u_3$ to be used in the next iteration. This is done by again solving a Riemann problem using the acoustic p-u relations, but starting now from the previous p_2,u_2 and p_3,u_3 conditions found using the higher-order shock and expansion solvers. This leads to a new value for $u_2 = u_3$. Once this new value of $u_2 = u_3$ is found, the previous solutions for states 2 and 3 are completely discarded and a new higher order set of calculations of states 2 and 3 is made to the updated $u_2 = u_3$ values. This procedure has been found to be exceedingly robust and to converge very rapidly. The procedure is repeated until the normalized error between p_2 and p_3 is less than 0.001 or the iteration number is eight, whichever comes first. In most cases, the procedure was found to converge in two or three iterations. Again, increasing the iteration number and improving the accuracy further were found to make no perceptible difference to the solutions.

With the complete Riemann solution in hand, it now remains to select the region in which the cell boundary lies to calculate the flux across said boundary. Since the cell and zone boundaries slide, in general, the line followed by the boundary in question will usually not be vertical in figure 3. (We will refer to this line as the "world line" of the boundary in question.) If the world line of the boundary is within one of the zones 1, 2, 3, 4, or 5, the flux is simply calculated using the primitive variables for that zones. Component mass fractions (and transverse velocities, if a multidimensional solution were being carried out) are simply those of region 1 or 4, depending on whether the boundary world line is to the left or right of the interface.

If the boundary world line lies within an expansion wave system, an additional expansion integration is carried out exactly to the world line to generate a new set of primitive variables which are then used to calculate the fluxes. The other option would be not to perform the extra integration and to assign the boundary world line to one or the other of the zones bounding the expansion wave depending on whether the world line lay to the left or right of some defined "middle" of the expansion wave. The fluxes would then be calculated directly from the primitive variables in the chosen zone. We have found virtually no difference in the code performance between these two techniques. Nevertheless, we have continued to use the technique with the extra integration, since it is, in principle, more correct and adds only a fraction of one percent to the CPU time requirements of the code.

3.4 Boundary Conditions

Calculation of the boundary fluxes comprises two components. First, at each end of each zone, conditions (i.e., the state vector, U) are calculated in a "ghost cell" which lies just outside the zone. A brief discussion of the use of so-called "ghost" cells is appropriate at this point. At both ends of a zone, just outside the zone, one or more ghost cells are added to the chain of real cells which form the interior of the zone. The cell-center values of the ghost

cells are chosen so that a Riemann solution between the real and ghost cells straddling the zone-boundary reproduces the proper zone-boundary condition. The use of ghost cells is extremely convenient when higher-order interpolations/extrapolations must be made near the zone boundary, since these can now be done essentially in the same way as is done in the interior regions of the zones. We now return to the main-boundary condition discussion.

Using the U values in the ghost cells, as well as those in the real cells of the zone(s), extrapolations/interpolations are made to the zone boundary. The fluxes there are calculated using Riemann solver techniques analogous to those used for the cell boundaries within a zone, as described in section 3.3. There is a certain degree of freedom in choosing the ghost cell values in a number of cases and this freedom becomes much greater when two ghost cells are used. For this reason, we have limited the code to the use of only one ghost cell and hence, second-order extrapolations/interpolations to the zone boundaries are used under some conditions. In addition, for some bc used only for code check-out, we have used cell-center (i.e., first order) values to calculate the zone-boundary fluxes. Below, we will briefly go through the bc used in the code.

For the infinitely stiff wall at zero velocity bc (bc #1), the ghost cell U (state variable) is created by taking the U of the last, adjacent real cell in the zone and simply reversing the velocity, i. e., replacing u by –u. For the point mass projectile bc (bc #10), the ghost cell U is created by taking the U of the last, adjacent real cell in the zone and replacing u by $2u_{proj}-u$, where u_{proj} is the projectile velocity. For the free surface bc (bc #2), the ghost cell U is created by solving a Riemann problem expanding to zero pressure. Solutions of all Riemann problems involved in determining the bc are done using the same techniques already described in section 3.3. There are three bcs are used for internal zone boundaries—moving boundary, different media (bc # 4); fixed boundary, same media (bc #5); and moving boundary, same media (bc #6). In all of these cases, the ghost cell Us are created by solving a Reimann problem between the two adjacent real end cells of the two zones. For some of the preceding bcs, some of the extrapolations/interpolations subsequently used to the boundary in question to calculate the boundary fluxes are of second order, rather than third order.

Four other bcs were used for code development and debugging work. The nonreflecting outflow condition (bc #3) sets the ghost cell U equal to that of the adjacent real cell. The supersonic inflow bc (bc #7) keeps the ghost cell U at a fixed value specified at the beginning of the CFD solution. In the subsonic inflow bc (bc #8), the ghost cell ρu and $H = e + p/\rho + u^2/2$ are kept at specified, fixed values and a Riemann solution is performed between the ghost cell and the adjacent real cell to determine completely the ghost cell U. Similarly, in the subsonic outflow bc (bc #9), the ghost cell p is kept at a specified, fixed value and a Riemann solution is performed between the ghost cell and the adjacent real cell to determine completely the ghost cell U. For all of the preceding four bcs, the extrapolations/interpolations subsequently used to the boundary in question to calculate the boundary fluxes are first-order (i.e., cell center) values.

For the blind end of the breech, bc #1 is used. For both sides of the piston, bc #4 is used. For the main diaphragm/projectile base condition, bc #1 is used before rupture. After rupture, bc #10 is used for point mass projectiles and bc #4 for projectiles with an internal zone and celling. For the free surface of an internally zoned projectile, bc #2 is used. If there is an extra diaphragm in the pump tube, bc #1 is used there before break and bc #6 after break.

3.5 Multiple Zoning

The computational domain is divided into several zones. Regions of different media, i.e., gunpowder (plus powder gas), polyethylene piston material, hydrogen pump-tube gas are always kept in different zones, to avoid the EOS difficulties that would occur if two different media co-existed in one cell. This problem is avoided by sliding the grids so that the grid zone boundaries move with the media boundaries. In some cases, more than one zone can be used for a single media, in particular, with the pump-tube gas. The gridding zones must, of course, change size in "accordion" fashion to follow the expansions and contractions of the media zones as the gun cycle progesses.

The cell sizes are arranged so that across a zone boundary, the zone end cell sizes are equal. This is done as follows. Every second zone has its cell sizes calculated at each time step independently of all other zones. Then the remaining zones have their end cell sizes calculated to match the end cell sizes (already calculated) immediately across the zone boundaries. Three methods of calculating the cell sizes are available for the first set of zones (calculated independently of all other zones). The first two are: (1) uniform cell sizes and (2) cells increasing (or decreasing) in size by a given, constant ratio from one end to the other of the zone. Method (3) is a combination technique. A critical cell size is chosen. If the zone length divided by the number of cells is less than this size, uniform cell sizing is chosen. If it is greater than this length, the cell size at a chosen end of this zone is set to the critical size and, moving away from this cell, the cell sizes successively increase by a ratio chosen to exactly fill the zone with cells. This ratio varies with every timestep. The

purpose of this complex zoning technique is (a) to allow such a zone to keep a reasonably small cell size (to obtain adequate resolution) at one end when the zone is greatly expanded and (b) to avoid extremely tiny cells and the consequent great reduction in code timestep when the zone is greatly compressed.

The remaining zones are calculated either by method (4) or method (5), as follows. In method (4), if the zone is an end zone, it is calculated with geometrically increasing (or decreasing) cell sizes from one end to the other (constant size ratio between adjacent cells). By adjusting the size ratio between adjacent cells, the cell size at the end of the zone abutting the neighbor zone can be adjusted to match that of the end cell of that zone. This size ratio varies with every timestep. If the zone is between two other zones, the previous technique does not provide sufficient degrees of freedom to match the end cell sizes across both zone boundaries. This problem is resolved by using method (5)—zoning the region with two different subregions each with geometrically varying cell sizes with two different size ratios between adjacent cells for the two regions. With two different size ratios available to vary, one can match the end cell sizes across each zone boundary of the zone and across the boundary between the two subregions.

The type of zoning must be selected by the program operator. For a three-zone (gunpowder, piston, and hydrogen) two-stage gun solution, good results have been found with the following zoning methods: gunpowder, method (4); piston, method (1); and hydrogen, method (4). For a four-zone (gunpowder, piston, hydrogen #1, and hydrogen #2) two-stage gun solution with an extra diaphragm in the pump tube between the two hydrogen zones (ref. 11) good results have been found with the following zoning methods: gunpowder, method (4); piston, method (1); hydrogen #1, method (5); and hydrogen #2, method (3).

3.6 Piston Jam Versus Bounce

The amount of friction calculated in the CFD code on the piston in generally not enough to prevent the piston from bouncing back after maximum gas compression. For our operating conditions of the NASA Ames 1.5 in. gun, it is observed that the piston, in fact, jams in the high-pressure coupling rather than bounces. To account for this, an option is available in the code which changes the bc at the piston front to the infinitely stiff wall at zero velocity bc #1 in section 2.7 (on both sides of the zone boundary) when the velocity of the piston front reaches zero. Most of the two-stage gun solutions presented herein use this option. It will be shown that this option produces excellent agreement between theory and experiment. The behavior of the piston exposed to high pressures appears, as will be discussed at a later point, to be very poorly understood and to disagree very substantially with low speed measurements of the yield stress and Young's modulus of the piston material.

4 Code Validation Versus Analytical Solutions

The code validation consists of two parts—validation against analytical solutions and validation against data from actual two-stage gun firings. In this section, we will outline the validations performed against given analytical solutions.

4.1 Riemann's Shock-Tube Problem

The first-validation work is against analytical solutions for Riemann's shock-tube problem. Figure 6 shows (a) the initial configuration with the high-pressure driver tube, the low-pressure driven tube and the diaphragm and (b), the x-t wave diaphragm. Upon rupture of the diaphragm, an expansion wave system moves into the driver-tube gas and the incident shock wave, followed by the driver-driven gas interface moves into the driven tube. The incident shock wave subsequently reflects from the driven-tube end wall, as shown. As far as is shown in figure 6, the wave processes can be modelled exactly analytically and thus serve as an excellent test for the CFD code.

The Riemann problem modelled analytically and by the CFD code used ideal gases, included no wall-friction or heat-transfer effects and had the following parameters:

Molecular weight	= 2
Specific heat ratio	= 1.4
Temperature	= 700 K
Pressure	= 6.898×10^8 dynes/cm^2
Length	= 2100 cm

Driven tube/driven gas –

Molecular weight	= 29
Specific heat ratio	= 1.4
Temperature	= 295 K
Pressure	= 8.669×10^5 dynes/cm^2 (or fraction thereof)
Length	= 2600 cm

With Riemann's shock tube problem, we can compare the analytical and CFD code solutions for the (1) incident shock, (2) the driver rarefaction, and (3) the reflected shock.

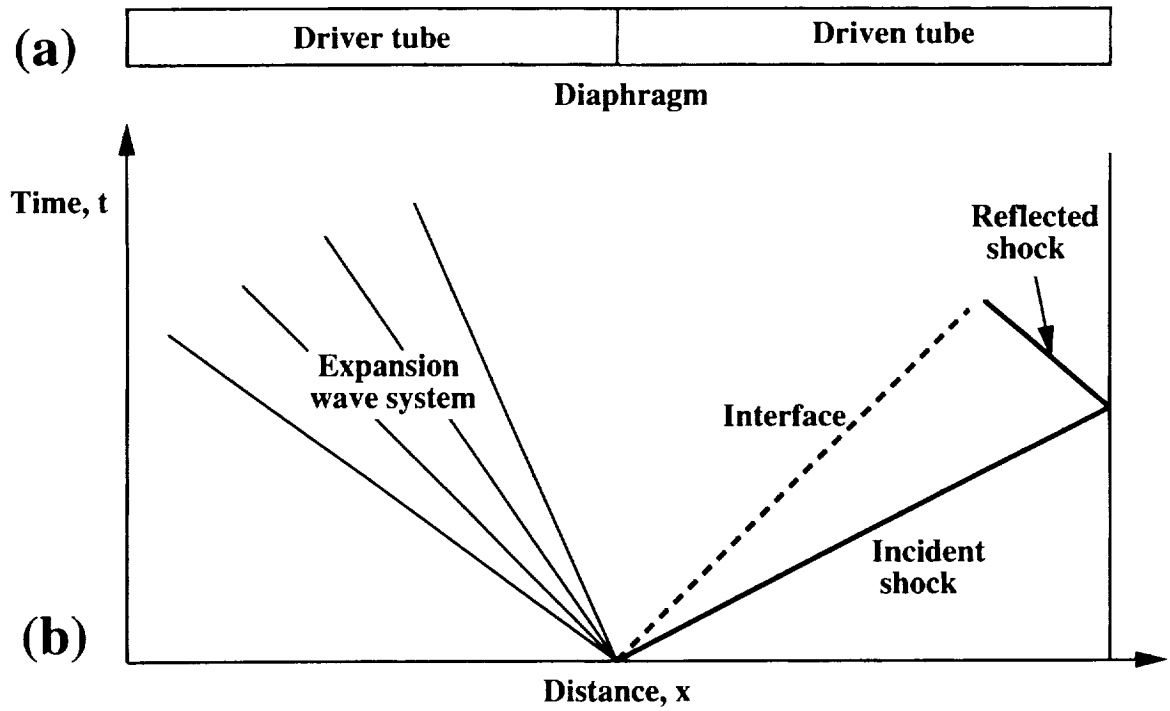

Figure 6. Riemann's shock-tube problem. (a) Shows initial configuration with driver and driven tubes and diaphragm; (b) shows x-t wave diagram.

CFD solutions were carried out with 20 cells each in the driver and driven tubes for the above pressure ratios (R_p) of (approximately) 10^3, and also, by reducing the driven tube pressure by successive factors of 10, for pressure ratios of (approximately) 10^4, 10^5, and 10^6. The solutions were then compared with exact analytical results. The CFD solutions were excellent at $R_p = 10^3$, showed modest deterioration at $R_p = 10^4$ and progressively more serious deterioration at $R_p = 10^5$ and 10^6. As an example of deterioration, the peak-to-peak amplitude of the pressure oscillations behind the incident shock in the Riemann shock tube problem was 1–2 percent for $R_p = 10^3$ and 10^4, 10 percent for $R_p = 10^5$ and 40 percent for $R_p = 10^6$. Nevertheless, the code was robust in that it produced solutions at R_p up to 10^6 with only 20 cells per zone, and that the degradation of the solutions as R_p increased from 10^4 to 10^6 took place in a smooth, consistent fashion. The number of cells per zone was then increased to 40 and to 80. With 80 cells per zone, the solutions were now excellent for R_p of 10^4, and the rather large entropy (temperature) errors of the solutions for R_p of 10^5 and 10^6 with 20 cells per zone were much reduced. For example, (spurious) oscillations in temperature in the reflected shock region for $R_p = 10^6$ were reduced from 67 percent to 17 percent when the number of cells was increased from 20 to 80. At the same time, the oscillations behind the incident shock referred to earlier were reduced from 40 percent to 12 percent (for $R_p = 10^6$). Finally, we switched from uniform cells in the driven gas to having these cells decreasing in size by a constant ratio from the end wall to the interface. With an overall decrease in cell size within the zone by a factor of 36, still further improvements in the solution for $R_p = 10^6$ were obtained. The CFD code issues discussed above regarding the Riemann shock tube problem are very similar to those presented in reference 34 for solutions with between 200 and 3200 cells (total).

4.2 Plate-Slap Problem

In this problem we consider two plates of polyethylene impacting each other at a closing velocity of 20 km/sec. One plate (the anvil) is initially at rest and is backed by an infinitely stiff wall. The rear surface of the moving plate (flyer) is completely free. Figure 7 shows (a) the initial configuration with the flyer, anvil, and infinitely stiff wall (b), the x-t wave diaphragm. Upon impact of the flyer and the anvil, shock waves are created in both. The anvil

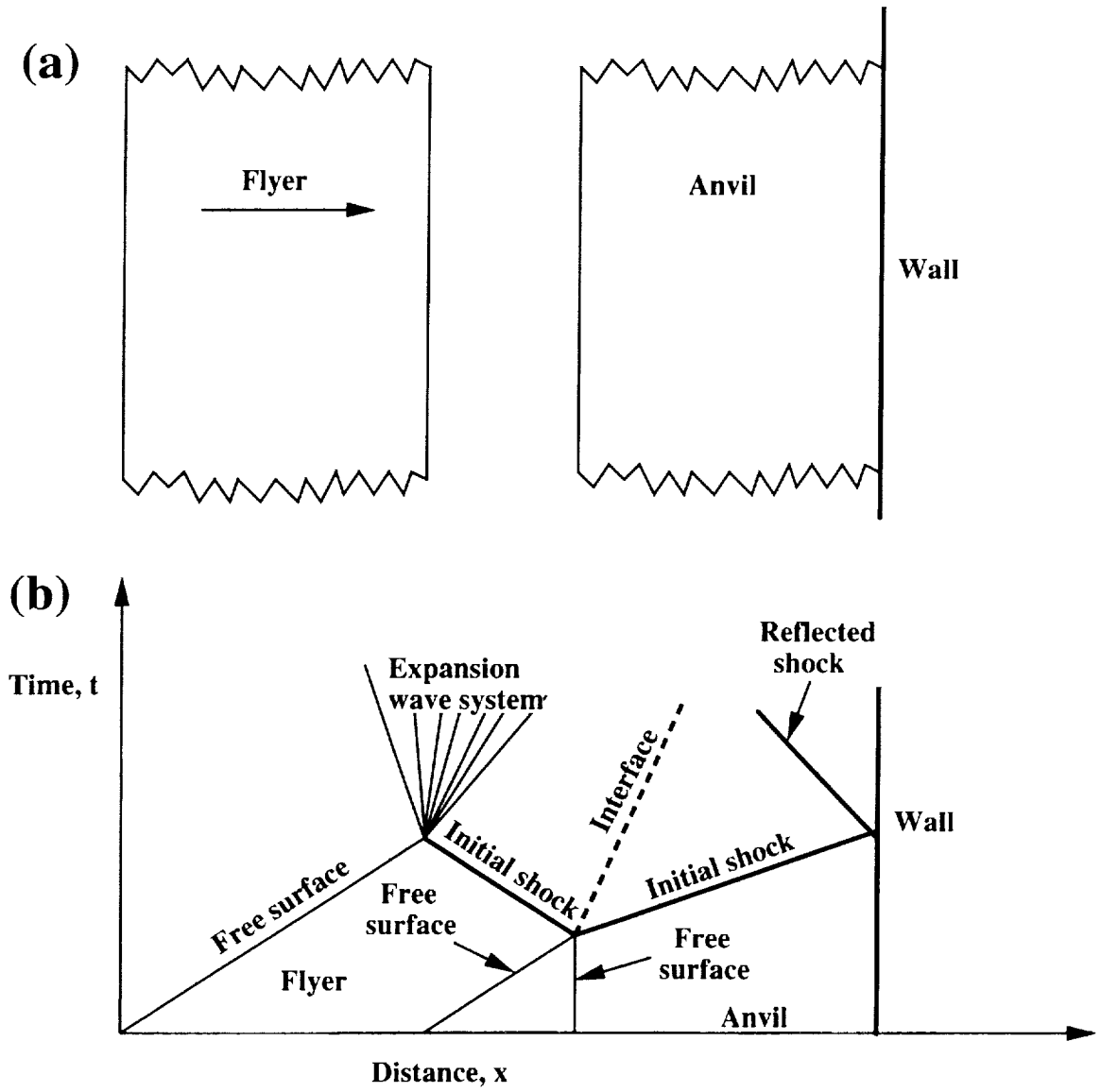

Figure 7. Plate-slap problem. (a) Shows initial configuration with flyer, anvil, and infinitely stiff wal;, (b) shows x-t wave diagram.

shock wave reflects as a shock wave from the infinitely stiff wall and the flyer shock wave reflects as a complete centered rarefaction wave system from the flyer free surface. Again, as far as is shown in the figure, the wave processes can be modelled exactly analytically and thus serve as an excellent test for the CFD code.

The dense media EOS #3 (see sec. 2.2) is used for the polyethylene. This test case allows study of (1) the initial pair of shock waves in both plates, (2) a shock wave reflected from the infinitely stiff wall, and (3) a complete expansion wave reflected from the free surface. Comparisons were again made between the CFD code solutions and exact analytical solutions. Solutions were carried out with a total of 40, 80, and 160 cells. The solutions were excellent, especially for the cases with 80 and 160 cells. Some small wiggles, of the order of 2–3 percent, were observed immediately downstream of shock waves, but quickly damped out, and some entropy errors (5–10 percent maximum density error) were created where the shock waves were created or reflected.

Otherwise, the solutions were very accurate, with all shock- and expansion-wave velocities and pressures very well predicted.

4.3 Convergent-Divergent Nozzle

In the preceding code validations, the cell area has been constant, i.e., the solution has been completely one-dimensional. To test the code with area changes, we examine steady, frictionless flow of ideal air through a convergent-divergent nozzle. The nozzle area decreases by a factor of 16 to the throat and then increases by a factor of 16 back to its original area. The total length of the portion of the nozzle with area variations is 32 cm and the nozzle diameter varies from 10 cm to 2.5 cm and then back to 10 cm. The CFD code calculation was done with 90 cells filled with air. Both air and cells are pushed through the nozzle by pistons located upstream and downstream of the nozzle. The air does not move with the same velocity as the cells, since this is not a Lagrangian code. The initial cell conditions are set to the exact quasi-one-dimensional solution and then about 40 cells are pushed through the nozzle. The solution is re-examined against the exact quasi-one-dimensional solution to assess code accuracy. (Some of the cells make a complete traverse of the portion of the nozzle with area changes.) The ideal pressure ratio across the nozzle is about 300 to 1 and the exit Mach number is about 4.5.

The errors were assessed primarily by evaluating the entropy and enthalpy throughout the nozzle. The maximum enthalpy (or temperature) error was 0.5 percent and the maximum entropy error was $\Delta S/R = 0.02$, which would correspond to a pressure error of 2 percent. This was judged very satisfactory for a nozzle with a pressure ratio of 300. With half as many cells, the errors are considerably larger, with a maximum enthalpy error of 2.7 percent and a maximum entropy error of $\Delta S/R = 0.17$.

4.4 Gunpowder Burn

Gunpowder burn in the CFD code within a closed bomb with 10 cells was compared with results obtained from a very highly accurate (small timestep) direct (non-CFD) integration of the powder-burn equations. In both calculations, the shape of the powder grain changes as it is consumed. All results agreed within 0.5 percent between the two sets of calculations.

4.5 Friction and Heat-Transfer Calculations

No simple analytical solutions are available against which to test the friction and heat-transfer calculations. However, special checks were made of the friction and heat-transfer calculations for gases and dense media and of the nonequilibrium turbulent kinetic energy calculation for gases, as follows. For each of these calculation techniques, for one cell, for one timestep, a complete hand calculation was made to six decimal places and the results compared with extensive special diagnostic print-outs from the CFD code. A few errors were found in this way and were corrected.

5 Code Validation Versus Actual Gun Data

Sections 5.1–5.5 discuss mainly code validation with experimental data from actual two-stage gun firings. Section 5.6 discusses mainly important predictions made by the code which we cannot, at present verify experimentally, such as the pressure histories in the high-pressure section of the gun and at the projectile base. Finally, section 5.7 discusses apparent anomalous yielding and deflection behavior of the pump-tube piston.

5.1 Gun Configuration and Operating Conditions

Figure 8 is a sketch (not to scale) showing the dimensions of the Ames 1.5 in. gun (with the benchmark piston) as modelled in the CFD code. The high-pressure coupling contraction is actually modelled with two cones with a slight break in the slope at the 3358.58 cm station at a diameter of 11.35 cm. This is not shown in figure 8 for clarity. However, using two cones models the actual measured contraction dimensions considerably better than if only one cone is used. Table 1 gives the benchmark operating conditions of the gun.

Figure 9 shows (a) the real piston and (b) the one-dimensional piston used in the CFD code.

The one-dimensional piston has the same land lengths and land and shank diameters as the real piston and its length has been adjusted so that its mass is equal to that of the real piston.

Table 2 summarizes the experimental and CFD data for a number of shots of the Ames 1.5 in. gun. The rupture pressures of the break valves (diaphragms) were calculated according to reference 35. Shots 600-607 (omitting shot 604) were at nominally identical gun operating conditions. The data from these shots were averaged to produce an "average" shot listed as "AV. 600–607" in the table. The powder-energy release, the powder-burn rate and the piston friction were adjusted to match the observed powder-chamber pressure histories and the piston velocity.

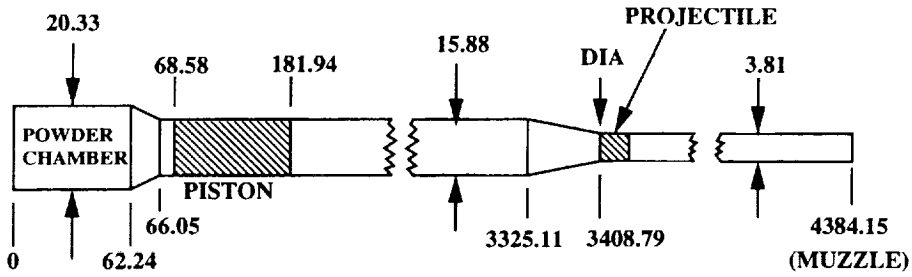

Figure 8. Gun modelled in CFD study. Not to scale. All dimensions are in centimeters. Station numbers are distances from blind end of breech. DIA denotes diaphragm (break valve).

Table 1. Ames 1.5 in. benchmark gun operating conditions

Powder	Hercules HC-33FS
Powder mass	3000 gm
Piston material	High-density polyethylene
Piston mass	21,420 gm
Pump-tube hydrogen pressure	3.104 bar
Break-valve break pressure	1216 bar
Sabot material	Lexan
Total launch mass	29.7 gm

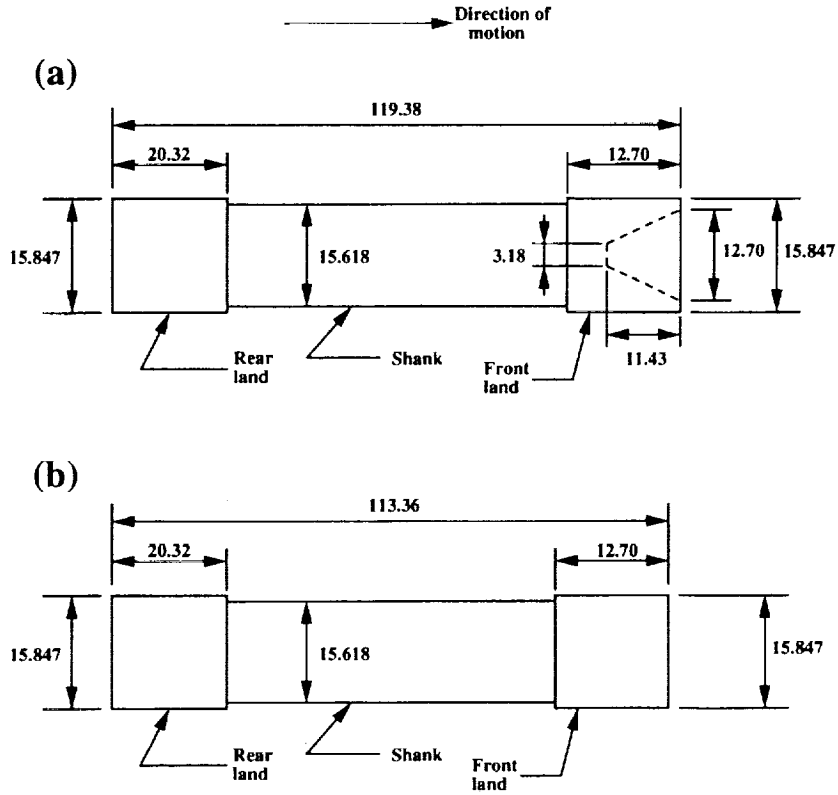

Figure 9. Representative pump tube piston for NASA Ames 1.5 in. gun (not to scale). Dimensions in centimeters. (a) Actual piston; (b) one-dimensional piston for CFD code.

Table 2. Experimental and CFD data for shots on NASA Ames 1.5 in. gun

Shot no.	Powder mass (gm)	Piston mass (gm)	Project. mass (gm)	Break valve press. (bar)	Hydrogen pressure (bar)	CFD piston velocity (m/s)	Exper. piston velocity (m/s)	CFD projectile velocity (km/s)	Exper. project. velocity (km/s)
600	3000	21,420	30	1216	3.104		684.5		6.605
601	3000	21,420	30.13	1216	3.104		683.2		6.765
602	3000	21,420	30.14	1216	3.104		685.3		
603	3000	21,420	30.3	1216	3.104		685.3		6.887
605	3000	21,420	29.81	1216	3.104		689.5		6.638
606	3000	21,420	29.68	1216	3.104		685.9		
607	3000	21,420	29.72	1216	3.104		685		6.714
AV. 600-607	3000	21,420		1216	3.104	685.8	685.6	6.744	6.722
613	2835	17,064	29.015	1216	3.104	742.8	735.9	7.002	6.818
614	2835	17,064	29.317	1216	3.104	742.8	735	7.002	6.829
615	2810	17,064	29.987	690	3.104	739.4	728.1	6.951	6.307
616	2835	17,064	29.57	813	4.711	710.3	716.1	7.092	7.217
618	2835	17,064	33.579	785	4.711	710.3	721.8	7.064	7.059

Table 3. Selection of powder and piston parameters

Gun	Ames 1.5 in.	Ames 0.28 in.
Powder		
Maker	Hercules	Du Pont/IMR
Type	HC-33FS	4227
Energy factor	0.97	0.97
Burn rate factor	1.891	1.581
Piston friction model		
Lands included	No	Yes
Land diameter	N/A	0.235 × actual + 0.765 × bore
Friction coeff. factor	0.396	1

5.2 Selection of Powder and Piston Parameters

Table 3 shows the parameters chosen for the Ames 1.5 in. and 0.28 in. guns. In the "powder" section of the table, the first-two lines give the maker and the type of the powder. The next line gives the energy factor—this is the factor by which the powder energy release calculated from the manufacturer's data (see sec. 2.6) must be multiplied to fit the experimental data. Next is given the burn rate factor—this is the factor by which the powder burn rate given by the manufacturer (see sec. 2.6) must be multiplied to fit the experimental data.

As mentioned above, the powder energy release, the powder burn rate and the piston friction were adjusted to match the observed powder chamber pressure histories and the piston velocity. Matching of the powder-chamber pressure history was made to the pressure rise and to the pressure fall from maximum to about 1/3 of the maximum value. The adjustment of these parameters requires the insertion of "fixes" into the code and we will now outline the reasons why we believe these are necessary. The adjustment of the powder energy release is very small (3 percent) and is the same for both types of powder and may possibly represent incomplete burning of the powder. It is also necessary to point out that fits to the experimental data that are almost as good as those obtained here are probably obtainable with no adjustment to the powder energy release. It is suggested that the powder energy factor be taken to be between 0.97 and 1.0.

On the other hand, the burn rate parameter is much greater than unity (1.58–1.89) and is quite different for the

two powders studied. There is a feedback mechanism in that higher burn rates raise the powder-chamber pressure which, in turn, causes still further increases in the burn rate. Hence, a burn rate parameter increase from 1.0 to, say, 1.7 produces a much larger relative increase in chamber pressure. The upshot of this is, that if one uses the burn rates given by the powder manufacturers in the code, the chamber pressure bears almost no resemblance to that actually observed, yielding a peak pressure only half (or less) than that observed and a pressure history very unrealistically stretched out in time.

Two effects likely contribute to the increased burn rate (over that predicted using the powder manufacturers' specified constants in equation (10) in sec. 2.6) in our two-stage gun breeches. First, the maximum pressures in the breeches of Ames' two-stage guns range from 400–1000 bar, whereas in typical military gun systems, the maximum pressures are often 3000 bar or higher (ref. 36). The manufacturers' burn-rate parameters are obtained from closed bomb or strand-burner tests and they are usually made (ref. 30) to emphasize the pressure range of 600 to 2000–2700 bar which is more applicable to military weapons. Some of the gun propellants for which data is given in references 30 and 37 show anomalies in the pressure range of 400–1000 bar which would translate to higher burn rates at these pressures than those which would be predicted by the powder manufacturers' equations. This point is also discussed in reference 38. Stated another way, it is possible that the manufacturers' burn-rate expressions may not be very applicable to the relatively low breech pressures of our two-stage guns.

A second effect is that in guns, there is gas flow over the propellant grains and the resulting increases in convective heat transfer cause corresponding increases in the burn rate ("erosive burning") over those which would be measured in closed vessels and are the usual basis of the manufacturers' burn rate equations. This point is discussed further in reference 39. The benchmark burn rate in our code is the standard expression given by the powder manufacturer. Further, the code, by choice, does not include the calculation of any erosive burning effects. The burn rate must be increased substantially above that given by the powder manufacturer in order to match the actual observed powder-chamber pressure histories. This is likely a result of the two effects discussed above. The factors of rate increase ("burn rate factor") observed to produce good agreement between theory and experiment for the two powders used in the Ames 1.5 in. and 0.28 in. guns (see table 3) were 1.89 and 1.58. Based on these numbers, it is recommended, in fitting a new powder in a new gun using our code, that one start with a burn rate factor of about 1.75 and iterate in to make the experimental and CFD powder-chamber pressure histories and the piston velocities agree.

In addition, the piston motion in the pump tube was found, in general, to take place as though the piston friction was substantially less than that calculated as discussed in section 2.5 and Appendix C. The real piston behavior can be much more accurately modelled by adjusting parameters in the piston model. One may (1) reduce the land diameter to reduce the jamming forces, (2) remove the lands entirely, or (3) reduce the coefficient of friction of the piston material against the steel pump tube. As indicated in table 3, for the 1.5 in. gun piston, the lands were removed entirely and the coefficient of friction was reduced to 0.396 times the normal values which would be used according to the models of section 2.7 and Appendix C. For the 0.28 in. gun, the land diameter was reduced as indicated in the table, but the friction coefficient was not changed from its normal value. [One should note here that the (room temperature) land diameter is greater than the tube bore and the pistons are inserted into the pump tube after having been cooled in a freezer and then are allowed to come up to room temperature and expand and jam in the pump tube.] The two methods chosen to reduce the piston friction shown in table 3 differ for historical reasons only—there is no reason to prefer one over the other.

There are a number of major difficulties in modelling the piston friction. First, the piston land surface may melt, reducing the friction coefficient below that used in the model (sec. 2.5 and App. C). Second, the lands will wear away progressively, thereby reducing the land jam in the pump tube, over the course of the piston stroke. Both of these phenomena are very difficult to model. Third, there is considerable evidence (see sec. 5.7) that the high strain rate deflection and yielding behavior of the piston material is very different from that predicted using material parameters measured in low strain rate situations. These latter parameters are used in our model (following ref. 4), lacking any data on high strain rate deflection and yielding behavior of the piston material. In general, the experimentally observed behavior of the piston indicates a substantially lower friction drag force than that which would be calculated applying the model of section 2.5 and Appendix C, directly, without modification. For the two guns modelled, the piston of the larger gun requires a much greater modification (reduction) in the calculated piston friction force to match the experimentally observed data. This may be due to the greater relative precision and smoothness of both the piston surfaces and the pump tube bore. This would tend to occur since the surface finishes and manufacturing tolerances tend to be nearly constant, regardless of component size. Hence, for a gun bore which is about five times larger (the Ames 1.5 in. gun),

the surface finishes and tolerances, normalized to the gun dimensions, are about five times better.

To reduce the piston friction to obtain agreement between CFD and experimental data for a new gun using our code, it is suggested to reduce the piston land diameter and the piston material friction coefficient as discussed above and shown in table 3. Since there are wide differences in the amounts of friction reduction required to obtain a good match between CFD and experiment and since piston friction is so poorly understood, we do not recommend even a first guess of how much to reduce the friction coefficient to model a new gun. This must be determined on a case by case basis. We point out that in determining the burn-rate factor and the piston friction reduction to be used with our code for a new gun, both parameters must be varied to get good agreement between the CFD and experimental chamber pressure histories and piston velocities. Typically, about 10 runs must be made with well chosen parameters to obtain good matches. It is suggested that a single, well documented, gun operating condition be chosen against which to adjust the burn rate factor and the piston friction reduction and that thereafter, these parameters be kept constant (for a given gun and powder type).

The performance of the gun is very sensitive to the piston velocity and hence to the piston friction. Thus, the determination of the burn rate factor and the piston friction reduction, as discussed above, are very important to enable one to obtain good code predictions. It turns out that the performance of the gun is very insensitive to the method of calculation of projectile friction (within reasonable limits). We have made CFD runs with nominal projectile friction, twice nominal projectile friction and zero projectile friction and the muzzle velocities were essentially identical for all three cases. This is believed to be due in part to the fact that average pressures acting on the projectile are much larger relative to the friction forces than those acting on the piston. (For much of the piston stroke, the pressures on both sides of the piston are quite low.) A second effect is as follows. When the projectile friction is increased arbitrarily (say, doubled), the first part of its trajectory is traversed at a lower velocity, as expected. However, it then stays closer to the high-pressure gas reservoir for a longer time, permitting the pressure waves from the reservoir to catch up to it more effectively than if it moved off more rapidly (with lower friction). The result is that, with the increased friction, the projectile is accelerated more effectively in the later part of its in-barrel trajectory. The overall result appears to be a near independence of muzzle velocity over a fairly wide range of assigned projectile friction values (within reasonable limits), as mentioned above. The calculations presented herein for the Ames 1.5 in. gun were made with the projectile diameter set exactly equal to the barrel diameter, and this is suggested as a starting point when applying our code to a new gun configuration.

5.3. Code Validation with Data from the Ames 1.5 in. Gun

As mentioned in the preceding section, the powder energy factor, the powder burn rate factor and the piston friction were tuned to make the powder-chamber pressures histories and piston velocities, calculated using the CFD code, match those for the benchmark gun operating condition, which is that of the average of shots 600–607 (see table 2). From this table, we see that the CFD piston velocity, in fact, is within 0.3 percent of the mean experimentally observed value, as would be expected, since it was tuned to agree. Figures 10 and 11 show the experimental and CFD powder-chamber pressure histories. The experimental data is for shot 607. Figure 8 shows the pressure histories out to 22 msec and figure 11 shows the histories out to 62 msec with a logarithmic pressure scale. Bit noise becomes progressively more evident in the experimental data as the pressure decreases. The pressure difference corresponding to one bit is about 1×10^7 dy/cm^2. The horizontal "lines" in the experimental data of figure 11 are due to switching between several bit levels; with the very large number of experimental data points (15,000), the data points merge into apparently solid lines. The matching of the pressure histories by the adjustment of the powder parameters and piston friction was done only out to a time of about 15 msec. The excellent agreement of the pressure histories out to pressures an order of magnitude lower and times out to 62 msec represent part of the validation of the accuracy of the code.

An important validation of the code is the comparison of the experimental and CFD projectile muzzle velocities. These are given for the benchmark gun operating condition (the line marked "AV. 600-607") in table 2. The CFD and experimental results agree within 0.5 percent. It is important to realize that the CFD projectile muzzle velocity was not tuned in any way, as was the CFD piston velocity. It simply results directly from the CFD analysis.

The code was also validated by comparing CFD predictions and experimental measurements in the pump tube made at station 3179.1 cm (see fig. 8) in the tube. The measurements were made using a PCB model 119M39 pressure transducer and a Kistler model 566 charge amplifier, as were the measurements of the powder-chamber pressure. Figures 12 and 13 show the experimental and CFD pump-tube pressure histories. The experimental data is for shot 607. Figure 12 shows the pressure histories

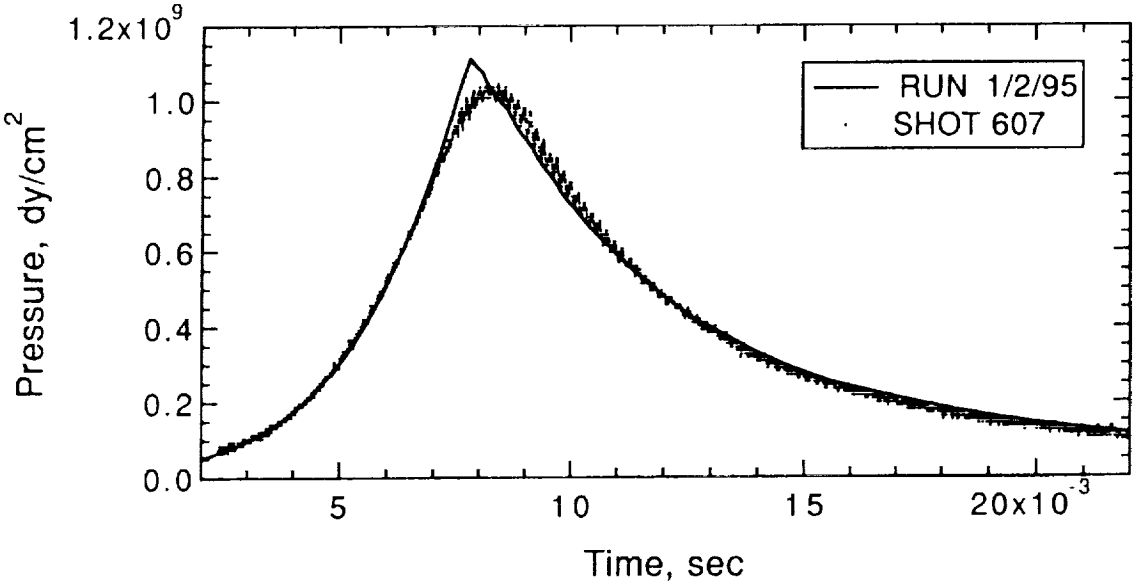

Figure 10. Experimental and CFD powder-chamber pressure histories.

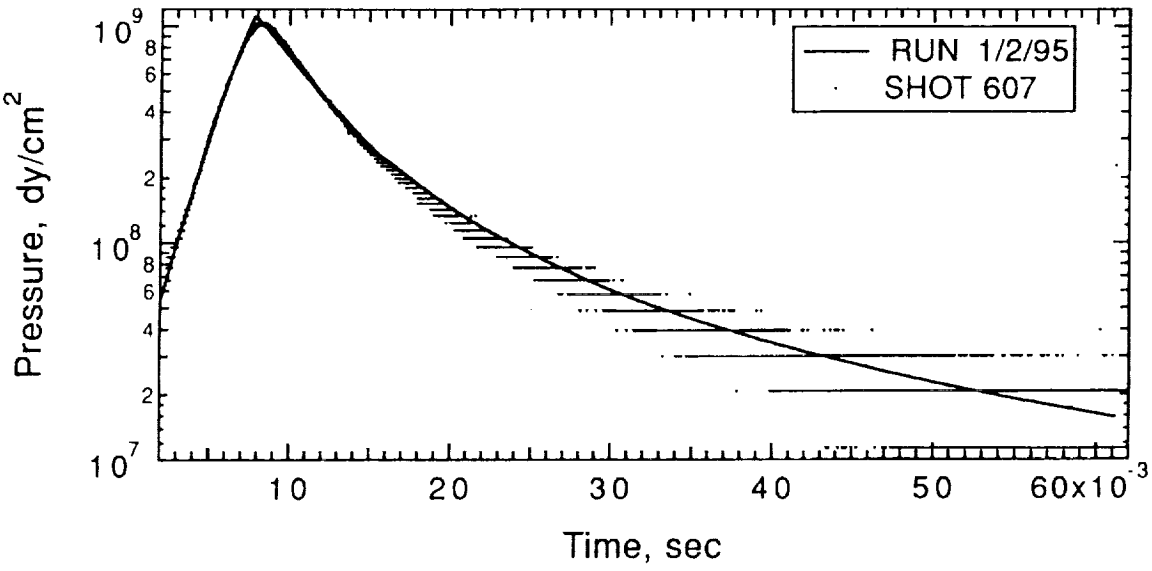

Figure 11. Experimental and CFD powder-chamber pressure histories.

from 20 to 65 msec with a logarithmic pressure scale and figure 13 shows the histories from 48 to 57 msec. Bit noise is particularly evident in the lower pressure ranges of figure 12. Six shock waves appear in the experimental pressure trace up to the time that the piston covers the transducer and all six waves are very well predicted by the code, with timing errors of perhaps 1–1.5 msec for the first wave, 0.5 msec for the next two waves and 0.2–0.3 msec for the last three waves. Many details of the pressure history are very well captured, such as gradual pressure rises between waves 3 and 4 and 4 and 5 (between 49 and 54.5 msec) and the curved "hooked" shape of wave 5 (at about 54.8 msec).

The experimental pressure levels are consistently about 15 percent higher than the predictions. It is believed that this is a transducer calibration problem, rather than any

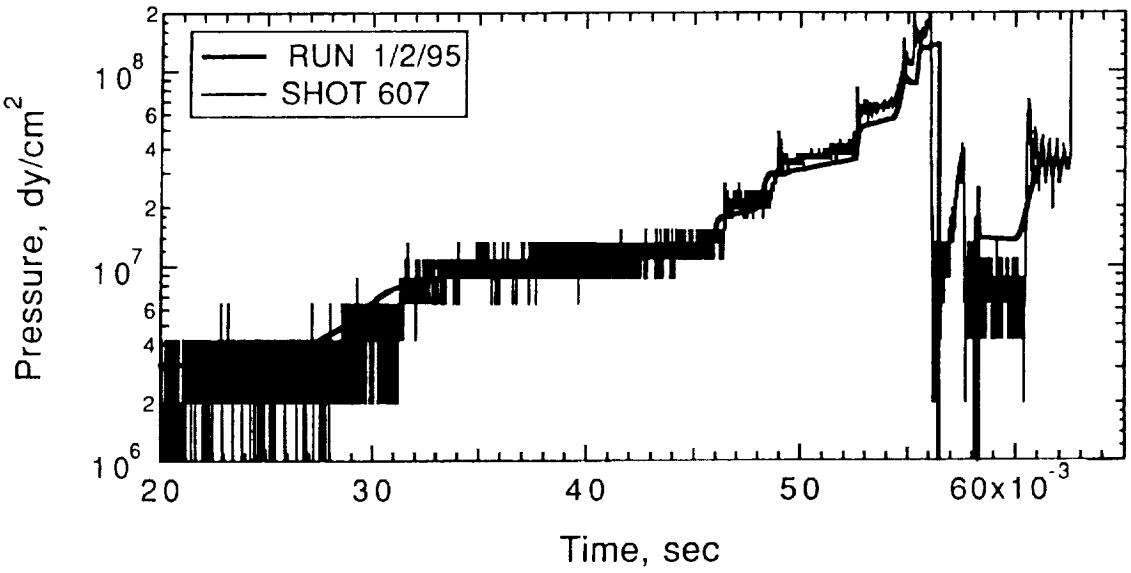

Figure 12. Experimental and CFD pump-tube pressure histories.

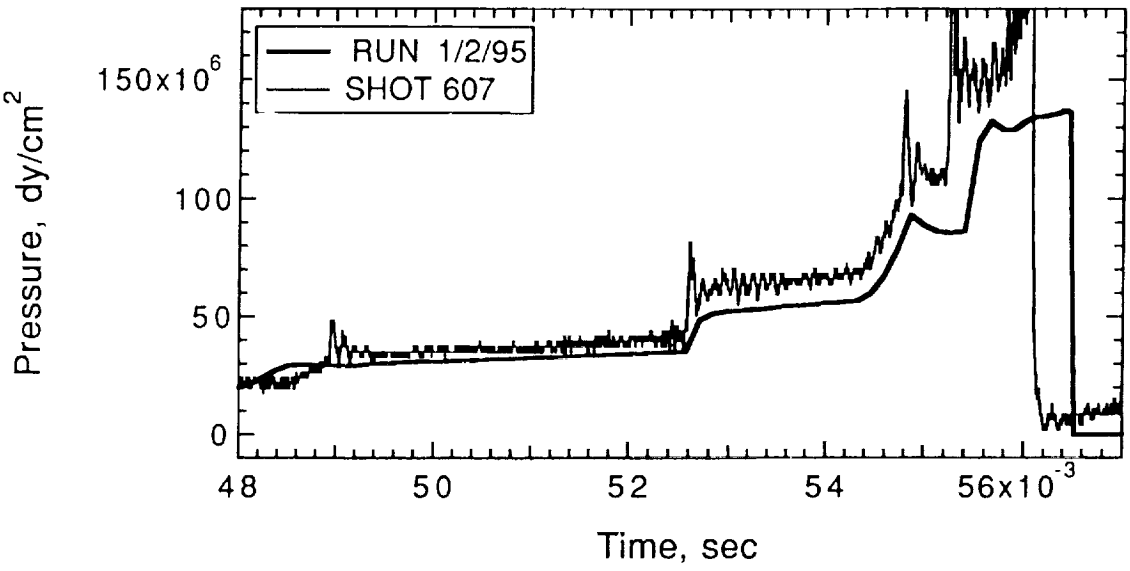

Figure 13. Experimental and CFD pump-tube pressure histories.

code difficulty. For example, if the code were that far off, the timing of the waves would be very much in error and other predictions of the code, such as projectile muzzle velocity, would also be substantially in error. The tranducer calibration factor could be in error because (1) we are using a 6900 bar transducer at a maximum pressure of 150 bar, and it is known that over such a wide pressure turn-down ratio, there can be some changes in the transducer calibration factor and (2) we are using an unconventional transducer measuring system, with a PCB transducer and a very old Kistler charge amplifier. It is possible that there is some uncertainty in the capacitance of the system, which would alter the transducer calibration factor. It would obviously be desirable to do a head-to-tail

in situ calibration of the transducer set-up, but neither time nor money to perform this has been available to date.

The code also makes predictions of where the pump-tube piston ends up in the converging high-pressure section of the gun. The real piston initially has a conical hole in its forward end, as shown in figure 9(a). By the time the piston ends up jammed in the high-pressure section of the gun, this hole is very much elongated and the forward end of the piston typically separated into several fingers. We have measured the final dimensions of two pistons and from these have determined the axial stations (in the co-ordinate system of fig. 8) of (1) the ends of the solid parts of the pistons and (2) the ends of the plastic fingers. Figure 14 is a sketch of one-half of the high-pressure section of the gun, in which are shown the experimentally measured stations of the piston data and the CFD prediction of the final position of the end for the one-dimensional solid piston. (The two experimentally measured positions of the ends of the fingers fall on top of each other in fig. 14.) The code prediction is excellent, in that it falls roughly mid-way between the experimentally observed ends of the solid part of the piston and the ends of the fingers.

The comparisons of the CFD and experimental data for the Ames 1.5 in. gun presented up to this point have been for one operating condition, that of the average of shots 600-607 in table 2. In the current test series, the gun has been fired at several other operating conditions (i.e., for shots 613–618) and data for these shots (excluding shot 617) are presented in table 2. Below, we make some limited comparisons from the data for the benchmark mean condition ("AV. 600–607") and shots 613–618 in table 2. (We note here that for shots 616–618, two sections of pump tube were removed, reducing the pump tube volume by about 33 percent and the pump-tube fill pressure was increased to maintain the same mass of hydrogen as for shots 600–607.) Figure 15 shows the comparison of the CFD and experimental piston velocities for these six conditions, along with the ideal perfect agreement line. The agreement is very good. The predictions are, of course, tuned to agree at the 685 m/sec point. For the other five data points, the errors are 0.8–1.0 percent (6–7 m/sec) for three points and about 1.5 percent (11 m/sec) for two points.

Figure 16 shows the comparisons of the CFD and experimental projectile muzzle velocities for the five of the six test conditions for which piston velocity data is shown in figure 15. The comparison for shot 615 is not shown, for the following reason. For this shot, for reasons of availability, a diaphragm much thicker than usual was used. Upon disassembling the gun after the shot, it was apparent that, after rupture, the thicker diaphragm throttled the flow significantly just aft of the initial position of the projectile base. This is believed to be the reason for the very low experimental muzzle velocity for this shot (6.3 km/sec versus a CFD prediction of 6.95 km sec). Hence, the data for this shot is not shown in figure 16. For the usual diaphragms, there is no throttling effect, since adequate diaphragm relief is machined into the barrel for 1–2 calibers downstream of the diaphragm station.

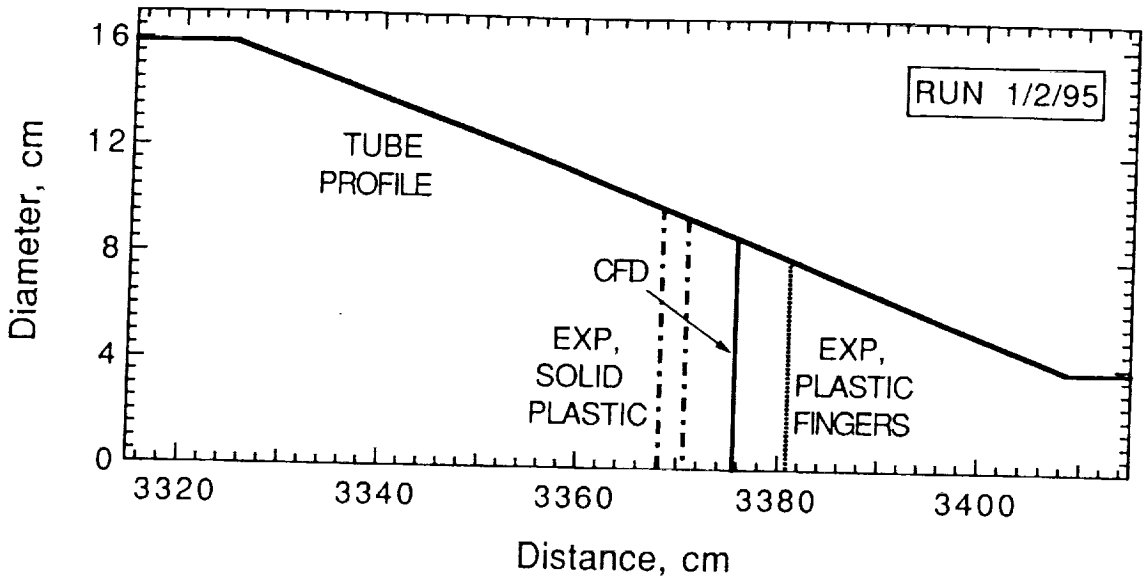

Figure 14. Experimental and CFD predictions of final position of end of piston.

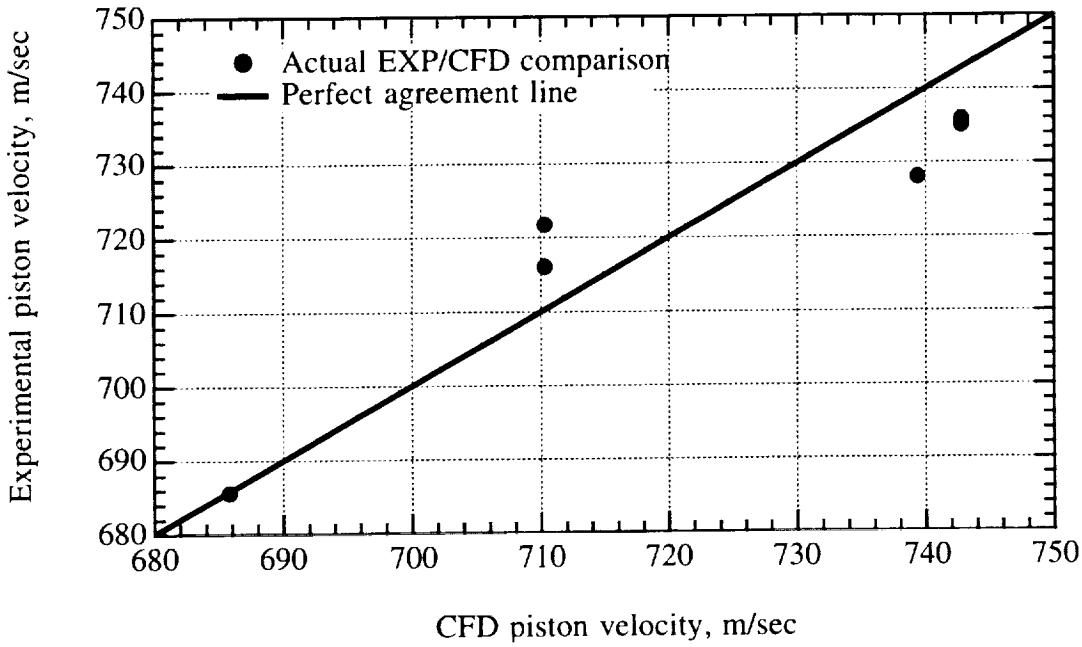

Figure 15. CFD and experimental piston velocities for the Ames 1.5 in. gun.

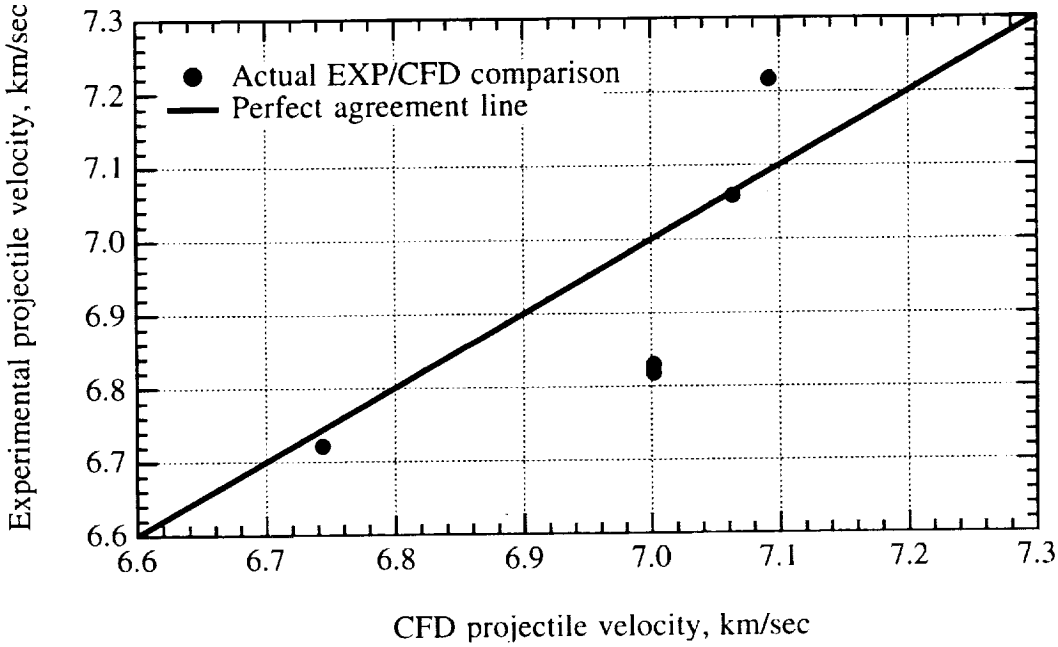

Figure 16. CFD and experimental projectile velocities for the Ames 1.5 in. gun.

The point at 6.73 km/sec is the point for the condition "AV. 600-607" in table 2. Agreement between theory and experiment is almost perfect for this point, as has been previously noted. The two points with experimental velocities of 6.82 km/sec (for shots 613 and 614) show velocity errors of about 3 percent (0.18 km/sec). For these same two points, the experimental piston velocities were about 1 percent low (see fig. 13). The muzzle velocity is known

to be extremely sensitive to the piston velocity and the 1 percent error in the latter velocity would lead to muzzle velocities 2–3 percent low. The remaining two data points show errors of 0.1 percent and 1.8 percent. Overall, the agreement between the CFD predictions and the experimental data was judged to be very good.

5.4 Code Validation with Data from the Ames 0.28 in. Gun

Data for a number of shots with the Ames 0.28 in. gun are given in table 4. A wider variety of gun operating conditions are represented here than for the data for the 1.5 in. gun (see table 2). Piston masses of 155, 205, and 222 grams and powder loads of 34, 40, and 50 grams were used. Three of the shots (shots no. 592, 594, and 596) had an extra diaphragm inserted in the pump tube to attempt to improve gun performance (see ref. 11). Projectile and piston velocities were not successfully obtained for all shots. The first CFD modelling using the present code was done for shots 577–579. However, the code contained an error at this point which caused an error in the projectile velocities, but did not affect the piston velocities. Hence, the comparison of projectile velocities is omitted for these three shots. The break valve rupture pressures shown in table 4 were calculated using the methods of reference 40. For the corresponding CFD calculations, these pressures were doubled in an attempt to allow for increases in yield and ultimate strength due to high strain rate effects (see, for example ref. 41). This is now no longer our preferred method of calculating rupture pressures of the break valves. We now use, instead, the method of reference 36 (as mentioned earlier) and use the value so calculated directly (without doubling) in the CFD calculations.

Figure 17 shows the comparison of the experimental versus CFD piston velocity data from table 4. Overall, the agreement, over a wide range of operating conditions, is very good. Eight data points are shown; for five of the points, the errors are less than 2.5 percent, one point has an error of 3 percent and two points have errors of about 4 percent.

Six sets of projectile velocity data are shown in table 4. For two of these shots (shots 592 and 593), the experimental velocities are very low, nearly 1 km/sec below the CFD predictions. These two projectiles were known to have somewhat undersize diameters and it is believed that this resulted in massive gas blow-by past the projectiles and, hence, the low muzzle velocities. The projectile diameters for shots 584 and 594–596 were much closer fits to the barrel diameter. The projectile velocity data for these four shots are plotted in figure 18. The experimental values run, in general, about 4 percent below the CFD values. To allow for this, we have plotted the line (experimental muzzle velocity) = 0.958 × (CFD muzzle velocity) on the graph (dashed line). The data points fall within 2 percent of this line, indicating that the code predicts the variations of gun performance quite well, once the overall 4 percent difference is allowed for. The 0.28 in. gun has a history of not shooting as well as other, larger, guns at Ames. This may, perhaps, be due to the occurrence of a certain amount of gas blow-by even for the best projectiles. This, is turn, may be due to the inevitably poorer machining tolerances and finishes which will occur, relative to the gun size, for a small gun, since these tolerances and finishes tend to have fixed absolute values.

Table 4. Experimental and CFD data for shots on NASA Ames 0.28 in. gun

Shot no.	Powder mass (gm)	Piston mass (gm)	Proj. mass (gm)	Break valve pressure (bar)	Hydrogen pressure (bar)	Pump tube dia. p. (bar)	Pump tube length (%)	CFD piston velocity (m/s)	Exper. piston velocity (m/s)	CFD project. velocity (km/s)	Exper. project. velocity (km/s)
577	34	204	0.334	517	1.52		100	665.8	666		
578	40	205	0.329	517	1.52		100	729.7	748.2		
579	40	155	0.324	517	1.52		100	819.5	800.7		
583	50	221	0.391	690	1.66		100	790.7	822.3		
584	50	222	0.371	690	1.66		100			7.134	6.741
585	50	222	0.398	690	1.66		100	785	822.1		
592	40	206	0.339	690	6.9	58.3	75	684.5		6.65	5.623
593	40	204	0.335	690	2.16		75	710.5	706.5	6.553	5.73
594	40	206	0.323	690	6.9	28.3	75	697.6		6.885	6.714
595	40	207	0.336	690	2.16		75	710.5	688.5	6.553	6.346
596	40	206	0.336	690	3.92/1.01	28.3	75	700.5	710.1	6.926	6.504

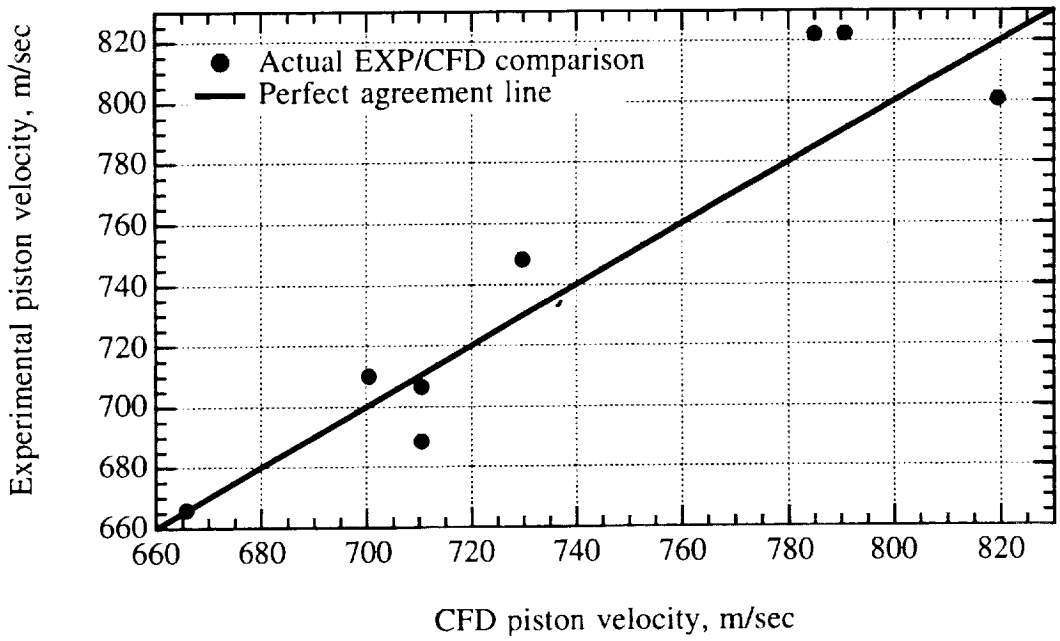

Figure 17. CFD and experimental piston velocities for the Ames 0.28 in. gun.

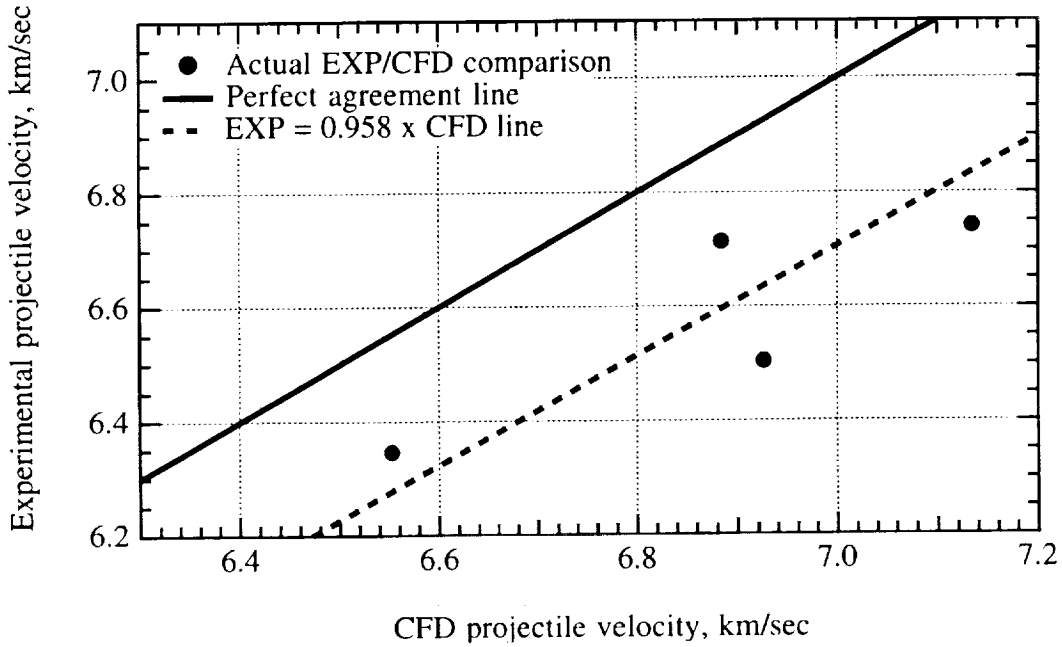

Figure 18. CFD and experimental projectile velocities for the Ames 0.28 in. gun.

5.5 Summary of Code Validation with Actual Gun Data

In this section, we sum up the validation of the code against experimental data from the Ames 1.5 in. and 0.28 in. guns. The validations were presented in detail in the two preceding sections. The first set of validations were for data at the benchmark operating condition of the Ames 1.5 in. gun (shots 600–607 in table 2). The validations consisted of comparisons of the following CFD and experimental data:

(1) pressure histories in the powder chamber,

(2) pressure histories in the pump tube,

(3) projectile muzzle velocity, and

(4) final position of end of pump-tube piston.

As described, agreement between the CFD and experimental data was excellent for all of these variables.

The second set of validations consisted of comparing CFD and experimental piston and projectile velocities for a number of different piston masses and powder loads for two very different guns—the Ames 1.5 in. and 0.28 in. guns. Data for a greater range of operating conditions were available for comparisons with the 0.28 in. gun. Very good agreement was found between theory and experiment for piston velocities. Projectile velocities were very well predicted (errors of 1–3 percent) for the Ames 1.5 in. gun. For the Ames 0.28 in. gun, the experimental projectile velocities were about 4 percent low. The small gun has a history of relatively poor performance and it is felt that this may be due to gun tolerance problems and possible blow-by of gas past the projectile which is not modelled by the code.

Overall, the validation of the code against actual gun data was judged to be very good.

5.6 Other Predictions of CFD Code

In this section, we present a number of code predictions which illustrate the usefulness of the code in (1) understanding phenomena within a two-stage gun and (2) choosing more favorable gun operating conditions (for example, lowering maximum gun and projectile base pressures while maintaining muzzle velocity). We are not currently able to make any direct measurements within certain key regions of our guns (i.e., high-pressure section and barrel), so the code's ability to give an "X-ray" picture of the internal fluid dynamics of the gun is very valuable for optimizing gun operating conditions. All of the predictions discussed in this section are from the CFD calculation for the benchmark gun operating condition of shots 600-607 in table 2.

Figure 19 shows CFD position and velocity histories of the front of the pump-tube piston. The piston accelerates in an s-shaped curve up to its maximum velocity of about 700 m/sec and then decelerates much more rapidly in the high-pressure section of the gun. As the piston enters the contraction section of the gun and is decelerating as a whole, there is some tendency for re-acceleration of the front end of the piston, due to the rapid area reduction. For the case of figure 19, this appears only as a small kink at a velocity of 540 m/sec, but for other, more violent operating conditions, this can result in a significant re-acceleration, for example, from 700 to 1000 m/sec.

Figure 20 shows the CFD pressure histories at two stations (3355.033 and 3380.127 cm) in the high-pressure section of the gun. These stations are located at about 35 percent and 65 percent of the way along the contraction (see fig. 8). A series of waves reflects between the front of the piston and the diaphragm (or the projectile base, after diaphragm rupture). These can be seen in the pressure histories of figure 20, up to pressure levels of about 2000 bar (also in figs. 12 and 13). Note the very high (6000–7000 bar) pressures calculated to occur in the high-pressure section of the gun. Obviously, limiting the maximum pressures reached here (and elsewhere in the gun) would be very desirable to obtain long component lifetime. By a judicious selection of gun operating conditions, it is possible to reduce the maximum pressures, while maintaining muzzle velocity, or, conversely, muzzle velocity can be increased while maintaining the maximum pressure levels in the gun.

Figures 21 and 22 show pressure snapshots at five different times during the gun-firing cycle. The two figures are identical except for the expanded time scale of figure 22. The three vertical dashed lines represent the position of the contraction of the high-pressure section of the gun. The outside two lines represent the beginning and end of the contraction (as modelled in the CFD code, see sec. 5.1) and the middle line in the slight break in the slope of the contraction. The intervals between the snapshots are not equal, but are about 0.6, 0.3, 0.3, and 0.4 msec. The projectile base is at the right end of the curves. We note again the very high maximum pressures (6000–7000 bar) for the second and third curves (c.f., with fig. 20). For the first four curves, there is a roughly linear slope on the left-hand side of the curves. This represents the piston, with the rear of the piston being at essentially zero pressure and the front face of the piston at the maximum pressure point. The roughly uniform pressure gradient over the length of the piston causes the piston to slow down very rapidly (see fig. 19). Note that the snapshots in the time period of the highest pressures show a pressure drop by about a factor of two from the high-pressure reservoir to the start of the barrel (at about

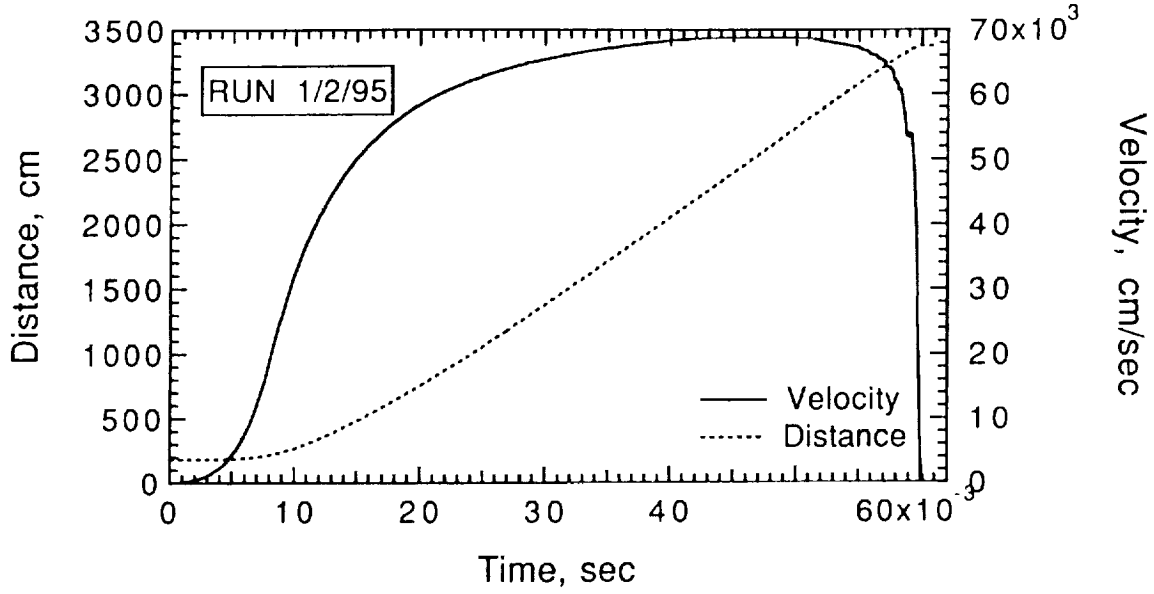

Figure 19. CFD predictions of velocity and position histories of front of piston.

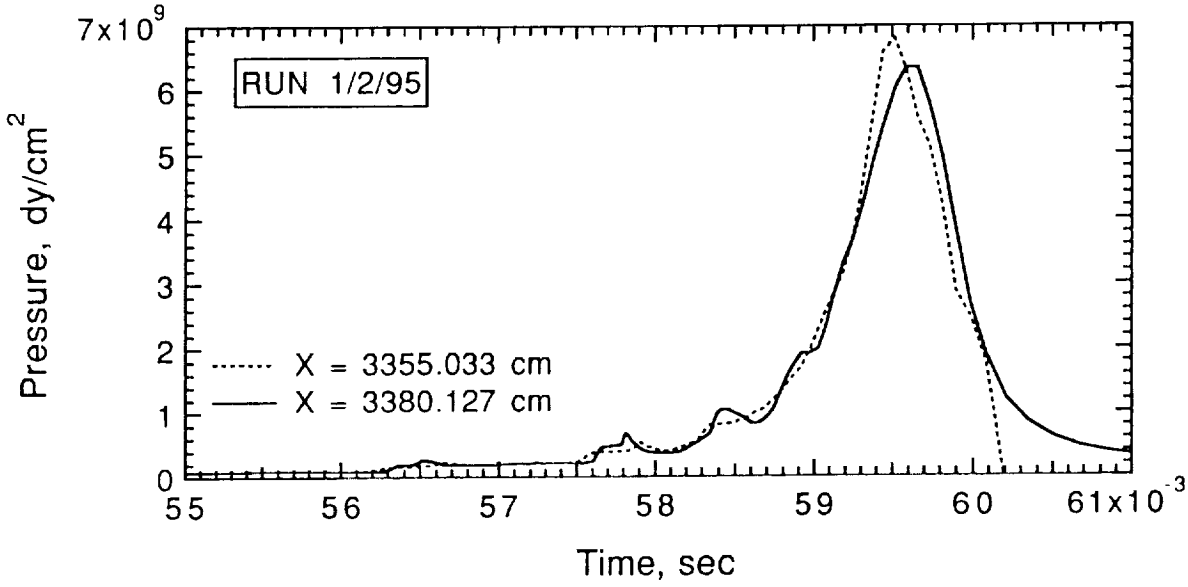

Figure 20. CFD predictions of pressure histories in high-pressure section of gun.

station 3410 cm). This is due to the start of the barrel acting as a sonic throat. The pressure at the projectile base is calculated to be much less than the maximum pressures in the high-pressure section of the gun (i.e., 1000–1500 bar maximum versus 6000-7000 bar). Finally, in the first four curves and, in particular, for the third and fourth curves, pressure waves can be seen in the barrel running between the piston front and the projectile base.

Figure 23 shows the pressure histories in the most forward hydrogen cell (solid line) and at the projectile base (dotted line). This hydrogen cell in question is adjacent either to the break valve (diaphragm) of the projectile base. The two curves fall on top of each other for much of the time interval shown. A series of waves of increasing amplitudes oscillates back and forth between the front of the piston and the break valve until the diaphragm breaks at

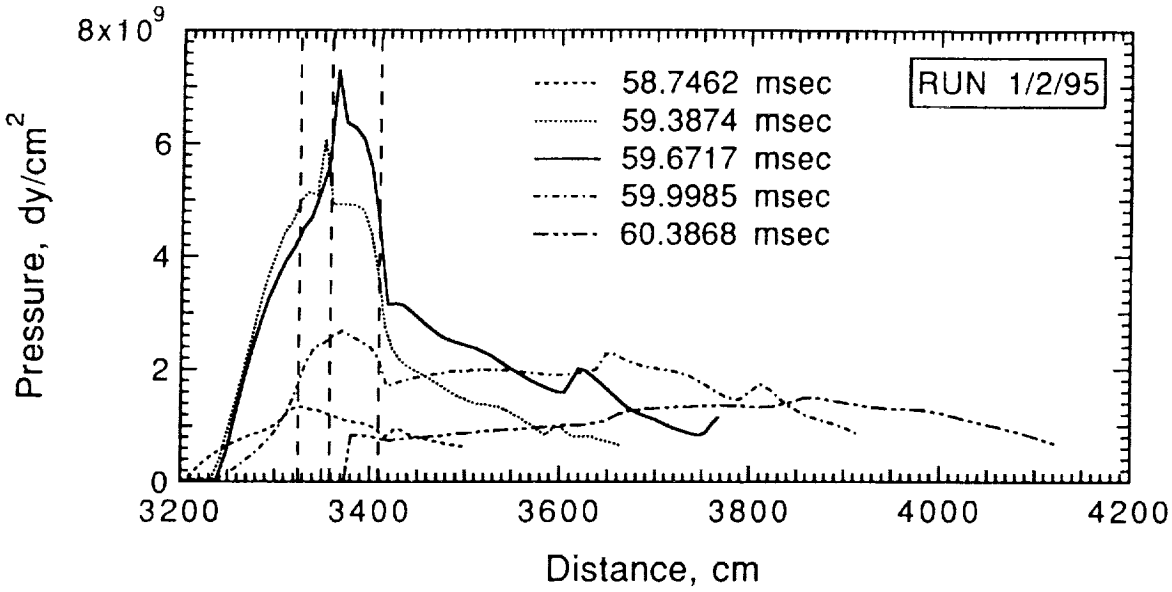

Figure 21. CFD predictions of pressure snapshots at several times in the gun.

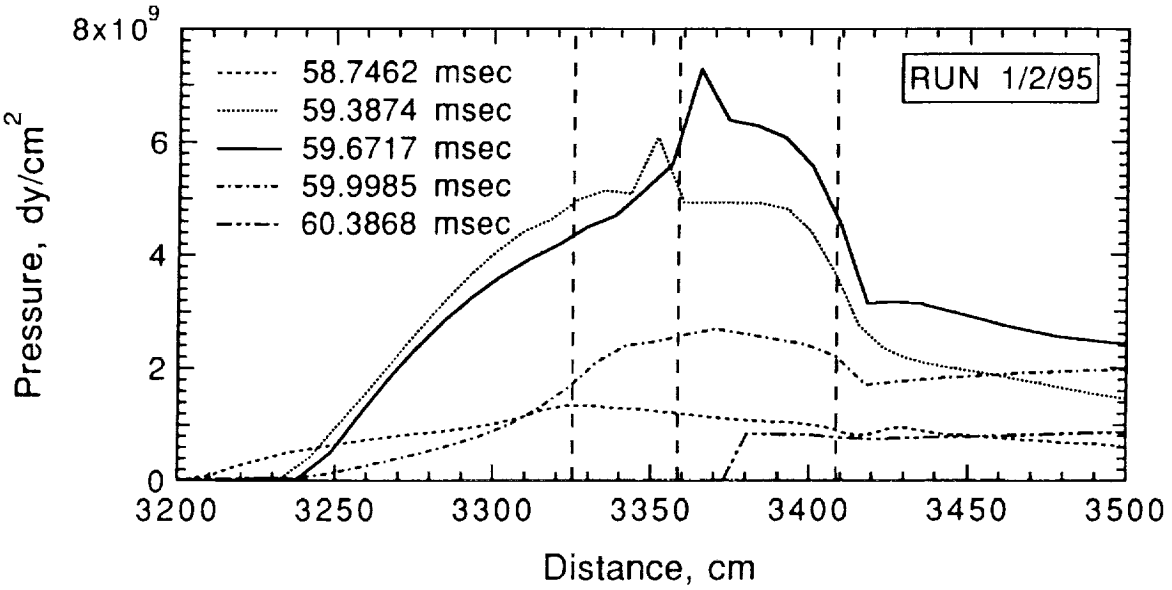

Figure 22. CFD predictions of pressure snapshots at several times in the gun. (As for fig. 21, but with expanded time scale.)

about 57.7 msec. Thereafter, the waves continue to oscillate between the front of the piston and the base of the projectile until about 60.1 msec, after which the projectile base pressure falls continuously. The effective average projectile base pressure over the length of the barrel is only about 700 bar, although with many spikes, the highest of which reach about 1600 bar. These very sharp spikes are separated by regions of much lower pressures (300–400 bar). This can be shown to be due the shock focusing action of the contraction section of the gun, which has an average full angle of about 8.7 deg. Using a much larger angle, such as 40 deg or 60 deg, will make the pressure history at the projectile base much more uniform.

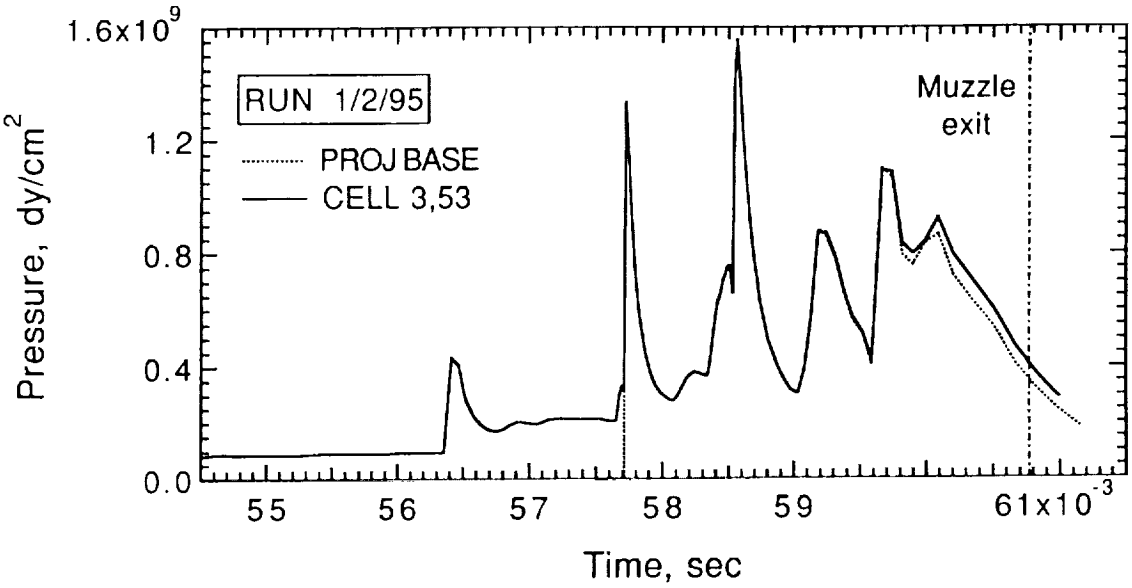

Figure 23. CFD predictions of pressure history at projectile base and in the last (most forward) hydrogen cell (cell 3,53).

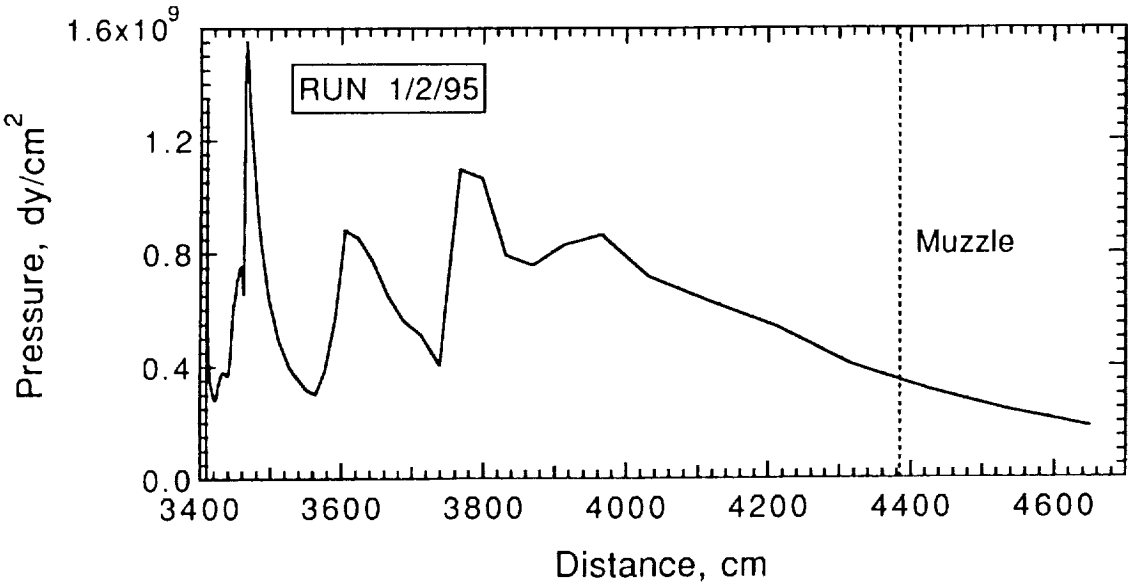

Figure 24. CFD predictions of projectile base pressure as a function of projectile position in barrel.

Figure 24 shows the projectile base pressure plotted as a function of the position of the projectile in the barrel. The same waves shown in figure 23 appear also in figure 24. From figure 24, one may determine the position of the projectile in the barrel when it was struck by the various pressure waves. Also, since (work) = (pressure) × (area) × (distance), the effective average projectile base pressure can be readily be determined as the mean pressure in figure 24, over the length of the barrel.

Figure 25 shows CFD position and velocity histories of the projectile. The steepest slopes of the velocity curves correspond to the arrival, at the projectile base, of the pressure peaks shown in figures 23 and 24.

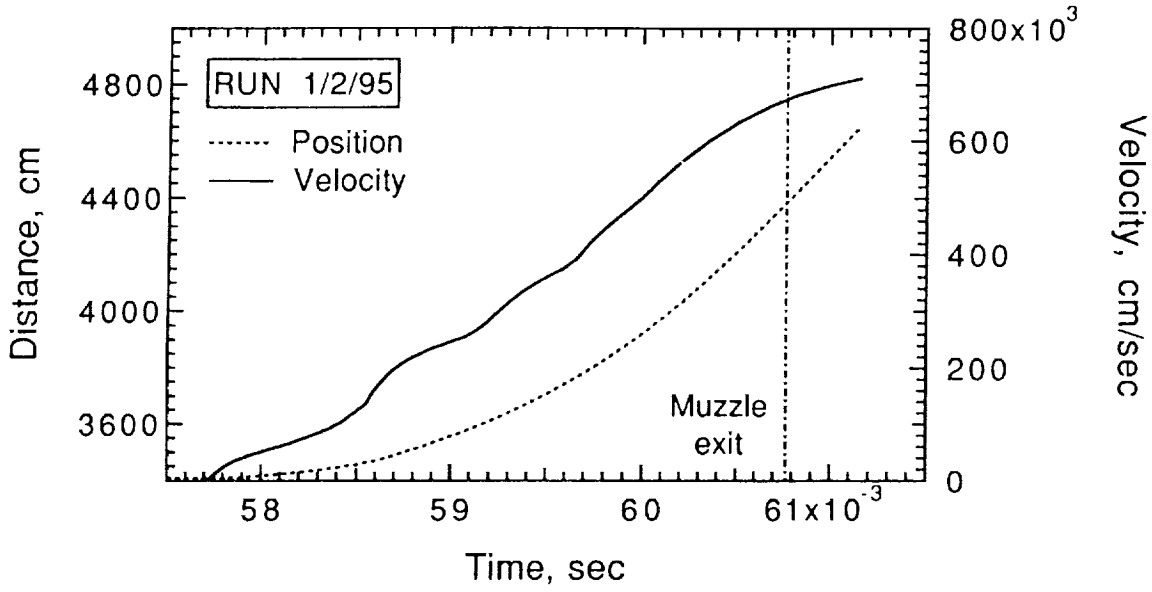

Figure 25. CFD predictions of velocity and position histories of projectile.

5.7 Discussion of Anomalous Piston Behavior

In this section, we discuss what appears to be very anomalous behavior of the pump tube piston. The piston shank diameter is considerably smaller than the tube bore (see figs. 8 and 9) being designed to ride free of the bore to reduce piston friction. However, following the model of section 2.5 and Appendix C (based on that of ref. 4), the shank should bear against the tube bore for part of the piston stroke cycle for the following reasons. The maximum powder-burn pressure is approximately 1000 bar (fig. 11) and portions of the shank should see axial pressures of up to 700 bar. The maximum hydrogen pressures are about 7000 bar (figs. 20–22) and portions of the shank should see axial pressures up to 4000–5000 bar. Now, the low strain rate yield strength and tensile modulus of elasticity (E) of polyethylene are given in a number of references (e.g., ref. 42) as roughly 200 bar and 9000 bar, respectively. From the longitudinal and shear sound speed and density data of reference 21 for polyethylene, using the equations of reference 43, we can deduce an E value of about 27,000 bar and a Poisson's ratio of about 0.4. Now, since the axial pressures in the shank very much exceed the stated yield strength at low-strain rate, based on the latter numbers, at least part of the shank should collapse and bear on the tube wall. Even if we assume that, at high strain rate, the yield strength of the piston is somehow very much increased above the low strain rate values, simply based upon elastic expansion of the piston under the applied axial pressure, the piston should expand laterally and bear against the tube wall.

However, upon examining a number of pistons after firing, we observe the following. The rear land clearly rides along the bore (as it must), and evidence of this is as follows.

(1) The land diameter is within 0.002–0.007 cm of that of the bore (some measurements being very slightly larger and others, very slightly smaller than the bore).

(2) The original circumferential machining marks are heavily worn down and, in some cases, removed.

(3) The land shows scratches and streaking in the axial (travel) direction.

On the other hand, the shank (except where it has been jammed into the contraction of the high-pressure section) shows absolutely no evidence of riding on the bore as indicated by the following observations.

(1) The shank diameter is consistently about 0.20 (or more) cm less than the bore diameter,

(2) The original circumferential machining marks remain undamaged.

(3) The shank shows no sign of axial scratches and streaking (except at the whisker gauge azimuth).

Thus, the piston appears to act as though both of the following are true:

(1) Its high strain rate yield stress is much higher than the quoted low-strain rate value.

(2) Its high strain rate tensile/compressive modulus is much higher than the quoted low-strain rate value (or alternatively that the high strain rate Poisson's ratio is much lower than the value of 0.4 derived from the data of ref. 21).

As noted in section 3.5, the piston would be calculated to bounce back after maximum gas compression if the bc at the front of the piston were not changed to stop the piston motion when the velocity of the front of the piston reaches zero. This was done in order to agree with the observed experimental behavior. This jamming behavior suggests that the high strain rate shear yield stress may be substantially higher than that estimated from the quoted low-strain rate tensile yield stress as described in Appendix C. If the high strain rate shear yield stress (and the friction coefficient) are sufficiently high, this would suffice to halt the piston naturally, without having to change the bc. The observed jamming behavior of the piston is thus, in a general way, consistent with the anomalous yielding and deflection behavior discussed above for the shank of the piston.

From the above discussion, there appear to be some very serious unresolved issues regarding high strain rate behavior of the pump tube piston and the modelling of same. We hope that the above discussion may perhaps, to a small degree, aid and stimulate the ballistics community towards the development of better modelling of piston phenomena.

6 Summary and Conclusions

We have presented a new code for the calculation of the performance of two-stage light gas guns. This code is based on the Godunov method and is third-order accurate in space and second-order accurate in time. The Riemann solver used is exact for shocks and uses a very accurate power law integration for expansion waves. Realistic EOS are used for all media. The code includes modelling of friction and heat transfer for powder gas, hydrogen, the pump-tube piston and the projectile. A simple nonequilibrium turbulence model is included for the gas flows and the predictions of skin friction and heat transfer to the tube walls in the gas flows are modified accordingly. Gunpowder burn in the first-stage breech is modelled using standard ballistic techniques.

The code was first validated with a number of analytical solutions. These included (1) Riemann's shock tube problem at pressure ratios up to 10^6, (2) impact of two polyethylene plates at a closing velocity of 20 km/sec, (3) flow through a convergent-divergent supersonic nozzle with an area ratio of 16 to 1, and (4) gunpowder burn in a closed bomb. All these code validations were found to be very good to excellent.

The code was then validated by comparing its predictions with experimental data from the Ames 1.5 in. and 0.28 in. light gas guns. These data included:

(1) powder-chamber pressure histories,

(2) pump-tube pressure histories,

(3) piston velocities,

(4) projectile velocities, and

(5) the observed final position of the front of the pump-tube piston.

To model the powder-chamber pressure histories and the piston velocity properly, it was found to be necessary to do the following:

(1) increase the burning rate over that given by the powder manufacturer by 60–90 percent and

(2) reduce the pump-tube piston friction below that predicted by direct, unadjusted application of the piston friction model.

Reasons for these changes and the way in which the parameters were modified were discussed in depth. After the powder burn rate and the piston friction were adjusted for one standard operating condition of each gun, they were then held constant for all other operating conditions. Predictions of the CFD code and the experimental measurements were in very good agreement for two very different guns (the Ames 1.5 in. and 0.28 in. guns), over a considerable range of operating conditions (particularly for the 0.28 in. gun).

Predictions of the code for the piston and projectile position and velocity histories for the 1.5 in. gun were presented. Calculated pressure histories and snapshots in the high-pressure section of the gun and at the projectile base were also presented. Discussion of these histories showed their usefulness in optimizing gun operating conditions, for example, to maximize muzzle velocity while maintaining given maximum gun pressures or, conversely, to reduce the maximum gun pressures while maintaining muzzle velocity.

Finally, observations made on pump tube pistons after firing strongly suggest that the high strain rate yielding and deflection behavior of the pistons in the pump tube is very different than that which would be predicted using low-strain rate data. It is suggested that considerably more work in this area may be necessary to allow improved predictions of piston behavior to be made.

APPENDIX A

Gas-Phase Friction and Heat Transfer

We start this analysis with well known (ref. 18 and 19) skin friction correlations for pipe flow. To correct for the effects of Mach number (M) and the difference between the wall temperature (T_w) and the average stream temperature (T), we use the correlations developed by van Driest (ref. 20). We have developed a "reference temperature" technique which reproduces the variations of skin friction coefficient, f (or C_f), with M and T_w/T given by van Driest's correlations within about 10 percent over a wide range of parameters without requiring the iterative solution of equations (66) or (71) in reference 20. We emphasize that our "reference temperature" is not the same as the usually used reference temperature (ref. 44). Our "reference temperature" (T') is given by

$$T' = 0.9T + 0.03M^2T + 0.46T_w \qquad \text{(A-1)}$$

We then evaluate the density and viscosity at the reference conditions

$$\rho' = \rho\frac{T}{T'} \qquad \text{(A-2)}$$

$$\mu' = \mu'(T', \rho') \qquad \text{(A-3)}$$

where ρ is the mean cell density. The basic, low pressure viscosities as functions of temperatures are fit using simple power laws to data from Golubev (ref. 45). This reference gives data for H_2, N_2, CO, CO_2, and H_2O. For the hydrogen pump-tube gas, the H_2 data is used directly. For the powder gas, the composition of the powder gas was taken from data sheets (ref. 46) provided by the powder manufacturer. The viscosity of the powder gas mixture at various temperatures was then found by adding up the individual viscosities from reference 45 multiplied by the mole fractions. The resulting gas mixture data was then fit with a power law curve. Golubev (ref. 47) gives density corrections for viscosity for H_2, N_2, and CO_2. These corrections as a function of density were fit with a sum of two terms with density ratios to two different powers and used to estimate a density correction for hydrogen and powder gas. Lacking pressure correction data for CO and H_2O, the data for N_2 and CO_2 was assumed to apply to CO and H_2O, respectively.

With ρ' and μ' determined, the Reynolds number (Re) for the cell in question is calculated as

$$Re'_D = \frac{\rho' uD}{\mu'} \qquad \text{(A-4)}$$

where u is the cell-center gas velocity and D is the mean diameter of the cell. The skin friction coefficient (ref. 18) for pipe flow as a function of Re is then fit with the following expressions

$$f' = 0.049\left(Re'_D\right)^{-0.2}, \qquad Re'_D \geq 5507 \qquad \text{(A-5)}$$

$$f' = 0.00875, \qquad 5507 \geq Re'_D \geq 1828 \qquad \text{(A-6)}$$

$$f' = \frac{16}{Re'_D}, \qquad 1828 \geq Re'_D \qquad \text{(A-7)}$$

for the turbulent, transition and laminar regimes, respectively. The skin friction coefficient is then corrected for nonequilibrium turbulence effects as follows

$$f'_{TC} = f'_{LAM} + \left(f' - f'_{LAM}\right)\left(\frac{TKE_{neq}}{TKE_{eq}}\right)^{0.5} \qquad \text{(A-8)}$$

where TKE_{eq} and TKE_{neq} are the equilibrium (steady-state) and nonequilbrium turbulent kinetic energies for the cell, f'_{LAM} is the laminar skin friction coefficient, always calculated from equation (A-7) and f'_{TC} is the final corrected skin friction coefficient. TKE_{neq} is calculated as shown in Appendix B. f'_{TC} is referenced to the density at the reference temperature; it is modified to refer to the mean cell density as follows

$$f = f'_{TC}\frac{T}{T'} \qquad \text{(A-9)}$$

The wall-friction force on the gas, F_{fr}, for the cell in question is then given by

$$F_{fr} = -\frac{1}{2} f\rho u|u|\pi D\Delta x \qquad \text{(A-10)}$$

where the wall area for the cell is $\pi D\Delta x$, with Δx being the cell length. Absolute value signs are required on one u term to maintain the proper sign of F_{fr}. To calculate the heat transfer from the gas to the walls, Reynolds' analogy (ref. 21) is used in the following form, which is correct if the Prandtl number is taken to be unity:

$$Q_w = \frac{F_{fr}}{u}(H - h_w) \qquad \text{(A-11)}$$

where H is the mean cell total enthalpy, h_w is the static enthalpy evaluated at the wall and Q_w is the heat-flow rate from the cell to the wall. The mean cell total enthalpy is related to the mean cell static enthalpy, h, by the usual relation

$$H = h + \frac{u^2}{2} \qquad \text{(A-12)}$$

Since h_w is not directly available as the cell center computational fluid dynamics (CFD) solution progresses, it is approximated as follows

$$\frac{h_w}{h} = \frac{T_w}{T} \qquad \text{(A-13)}$$

Combining equations (A-11)–(A-13) and using the relation between h, e, p, and ρ, we obtain, finally,

$$Q_w = \frac{F_{fr}}{u}\left[\left(e + \frac{p}{\rho}\right)\left(1 - \frac{T_w}{T}\right) + \frac{u^2}{2}\right] \qquad \text{(A-14)}$$

which is used to calculate the heat-flow rate from the cell to the wall in gas-flow regions.

For regions with gas and solids flowing together (gunpowder/powder gas), F_{fr} and Q_w are based on the density, enthalpy and sound speed of the gas only. The presence of solids is ignored. This two-phase flow situation applies only in the upstream part of the pump tube for the first part of the solution before all the powder is burned. Currently, T_w is prescribed and held fixed at 300 K. Estimates of the wall heating at various locations in the gun have been made. In most of the pump tube and the downstream part of the barrel, these effects are rather small. However, as is well known, in the high pressure coupling and in the upstream part of the barrel, wall heating is significant. However, the results of the code obtained to date are sufficiently good and useful even without wall-heating effects to warrant presentation in the current publication. At a later time, it is intended to modify the code to allow for wall-heating effects.

APPENDIX B

Gas-Phase Nonequilibrium Turbulence Model

A simple model is developed which assumes that the nonequilibrium turbulence kinetic energy (TKE) relaxes towards the equilibrium value for the flow in question (TKE_{eq}) with an e-folding length (L_e) which is a certain number of tube diameters. (The e-folding length is the length over which the difference between the nonequilibrium and equilibrium TKE will relax to 1/eth of its original value in a steady, constant area flow.) Hinze (ref. 22) presents an extensive discussion of the fully developed low speed turbulent pipe flow measurements of Laufer (ref. 23). We estimate L_e using (1) Laufer's graphs (presented in Hinze) of the TKE distribution across the pipe radius, (2) Laufer's graphs (also presented in Hinze) of the TKE production distribution across the pipe radius, and (3) Schlichting's (ref. 48) values for the ratio of maximum to mean velocity for low speed, fully developed pipe flow. From these data for $Re_D = 5 \times 10^5$, we estimate $L_e = 3.27 \times$ (pipe diameter). The range of Re for hydrogen flow in the pump tube is typically 3×10^5 to 3×10^7. The Re for the data of references 22 and 23 is within our range, but towards the low end of it. However, turbulent pipe flow does not appear to change very rapidly with Re over the Re range of interest (at least over the range 3×10^5 to 3×10^6 reported in ref. 24). Hence, we use the value of L_e given above as a rough estimate in our CFD model. The relaxation term in our model thus becomes

$$d(TKE) = \frac{dx}{L_e}\left(TKE_{eq} - TKE\right) \qquad \text{(B-1)}$$

where d(TKE) is the change in TKE which takes place when the flow moves a distance dx, and we use

$$TKE_{eq} = 0.00929u^2 \qquad \text{(B-2)}$$

also taken from the data of Laufer (ref. 23) for $Re_D = 5 \times 10^5$. For simplicity in the equations, we have dropped the subscript "neq" from TKE_{neq}; i.e., "TKE" in the present equations corresponds to TKE_{neq} in Appendix A. For one timestep dt, the distance that the flow moves is simply udt. Since the tube changes diameter in the gun model, L_e is not fixed, but is taken to be equal to $R_L D$, where $R_L = 3.27$, as discussed above. Inserting these two results into equation (B-1) yields the following equation for the relaxation term of the TKE equation

$$d(TKE) = \frac{udt}{DR_L}\left(TKE_{eq} - TKE\right) \qquad \text{(B-3)}$$

A difficulty with equation (B-3) is that, as it stands, there will be no TKE relaxation if the velocity, u goes to zero. Since the TKE will obviously relax due to the turbulent motion itself, even if u = 0, we have modified equation (B-3) by replacing u with $(u^2 + 2TKE)^{0.5}$ to yield our final form for the relaxation term of the TKE equation, as follows

$$d(TKE) = \frac{\sqrt{u^2 + 2TKE}}{DR_L}dt\left(TKE_{eq} - TKE\right) \qquad \text{(B-4)}$$

To calculate the changes of TKE within any cell over a timestep, equation (B-4) is used, along with the usual terms taking account of convection of TKE across the cell boundaries of cells. The nonequilibrium value of TKE thus calculated is then used to modify the skin friction coefficient as described in Appendix A.

Examination of the nonequilibrium and equilibrium TKE values calculated by the code shows the following. For the acceleration of the piston and the projectile, the TKE values are calculated to lag only slightly behind the equilibrium values, even during the very high initial accelerations of the piston and projectile. When the piston slows down very rapidly in the high-pressure section of the gun, however, the TKE in the rapidly decelerating gas in front of the piston is calculated to rise well above the equilibrium values. The inclusion of the nonequilibrium TKE model was found to make only minor changes (1–3 percent) in the code predictions of pressures and piston and projectile velocities.

APPENDIX C

Solid-Phase Friction and Heat Transfer

The method used is a variation of that presented in reference 4. We begin by calculating the normal stress between the solid body (piston or projectile) and the tube wall (σ_n) using the following logic and equations. Equations (C-2)–(C-7) are written in the form of two nested block IF FORTRAN statements.

$$\phi = \frac{E}{\sigma_y}\left[\frac{r_t}{r_p} - 1\right] \qquad \text{(C-1)}$$

IF $\phi > \mu$

$$\sigma_n = p_x - \sigma_y \qquad \text{(C-2)}$$

ELSE

$$\psi = -(1-\mu) \qquad \text{(C-3)}$$

IF $\phi < \mu$

$$\sigma_n = \sigma_y + \frac{\mu p_x}{1-\mu} \qquad \text{(C-4)}$$

ELSE

$$\sigma_n = \frac{-E\left(\frac{r_t}{r_p} - 1\right) + \mu p_x}{1-\mu} \qquad \text{(C-5)}$$

ENDIF

$$\text{If}(p_x - \sigma_n) \geq \sigma_y, \qquad \sigma_n = p_x - \sigma_y \qquad \text{(C-6)}$$

$$\text{If}(\sigma_n - p_x) \geq \sigma_y, \qquad \sigma_n = p_x + \sigma_y \qquad \text{(C-7)}$$

ENDIF

where:

- r_t = tube radius
- r_p = unstressed initial radius of solid material (outside tube)
- σ_y = yield stress of solid
- E = Young's modulus of solid
- μ = Poisson's ratio of solid
- p_x = axial pressure (from CFD code results)
- s_n = stress in solid normal to the x direction

In the above equations, since p_x is positive for pressures in the CFD code, we have taken σ_n to be positive for compression, which is the reverse of the usual strength of materials convention.

The above set of equations looks formidable but actually embodies a rather simple elastic-plastic model as follows. First, the normal stress on the solid (σ_n) is calculated assuming elastic behavior, taking into account the applied pressure in the x direction (p_x) and the initial jamming of the solid rod into the tube. If the difference $|\sigma_n - p_x|$ so calculated is less than the yield stress, σ_y, this value of σ_n is used unmodified. If $|\sigma_n - p_x| > \sigma_y$, then σ_n is set equal to $p_x \pm \sigma_y$, as appropriate. This represents the plastic conditions part of the model. The case where the solid rod is smaller than the tube (free), either initially (unstressed) or after the application of p_x, is allowed for in the above logic set.

Again following reference 4, the normal stress is limited as follows (so that it cannot become negative):

$$\sigma_n = \max(0, \sigma_n) \qquad \text{(C-8)}$$

A number of references 25–28 have discussed high speed models for dynamic sliding friction. Reference 26 points out that the experimental data of reference 25 for nylon on steel up to about 0.7 km/sec can be fairly well fit with a curve of the form

$$\mu_d = Au^{-0.4} \qquad \text{(C-9)}$$

where u is the relative velocity, A is a constant and μ_d is the dynamic friction coefficient. Reference 26 used equation (C-9) for studies of model wear in a two-stage gas gun. Reference 27 used the same equation for friction modelling in an electromagnetic launcher. In reference 28, equation (C-9) for the friction coefficient was generalized to the following expression for μ_f, at any velocity (including zero velocity),

$$\mu_f = \min\left(\mu_s, Au^{-b}\right) \qquad \text{(C-10)}$$

where μ_s is the static friction coefficient. We have used equation (C-10) recommended by reference 28 and have reevaluated the coefficients A and b directly from the data of reference 25 for nylon on steel. We have obtained b = 0.4224 and A = 8.377 (if the velocity is in cm/sec). From figure 242 of reference 25, μ_s is estimated as 0.185. Lacking dynamic friction data for piston and projectile materials such as polyethylene and Lexan, we have simply scaled the A coefficient in equation (C-10), obtained from the data of reference 25 for nylon on steel, by the respective static friction coefficients to make first estimates for the dynamic friction coefficients for the other materials.

With an estimate for the friction coefficient available, the wall-shear stress, τ_w, is calculated from the following two equations

$$\tau_w = \mu_f \sigma_n \tag{C-11}$$

$$\tau_w = \min\left(\tau_w, \frac{\sigma_y}{\sqrt{3}}\right) \tag{C-12}$$

Equation (C-11) is simply the basic friction relation and equation (C-12) limits the maximum possible wall shear stress to the shear yield stress, here taken to be $1/\sqrt{3}$ times the tensile yield stress, following reference 29. With τ_w available, the wall friction force on the solid in a given cell can be found simply by multiplying τ_w by the area of the cell in contact with the wall. The heat-flux rate to the solid, q_w, due to the solid friction work is simply taken to be one half the shear stress times the velocity, as follows

$$q_w = -\frac{1}{2}|\tau_w u| \tag{C-13}$$

This term, which appears as a source term in the energy equation, represents energy loss from the solid to the wall due to frictional heating occurring at the wall. The other half of the heat generated by the frictional work is assumed to flow to the solid and does not represent an energy loss from the cell and therefore should not be included in the energy equation. If a point mass projectile is assumed, the wall shear stress and heat-flux source terms are calculated midway along the corresponding (equal mass) real length projectile and multiplied by the proper wall-projectile contact area for the real length projectile.

References

1. Canning, T. N.; Seiff, A.; and James, C. S., eds.: Ballistic-Range Technology. AGARDograph 138, Aug. 1970.

2. Piacesi, R.; Gates, D. F.; and Seigel, A. E.: Computer Analysis of Two-Stage Hypervelocity Model Launchers. Naval Ordnance Laboratory, NOLTR 62-87, Feb. 1963.

3. Charters, A. C.; and Sangster, D. K.: Fortran Computer Program for the Interior Ballistic Analysis of Light Gas Guns. Unpublished manual to CFD code, 1973.

4. Nappert, L.; Lesage, F.; and Gottlieb, J. J.: Development and Experimental Validation of a Numerical Model for the Prediction of Two-Stage Light-Gas Gun Performance. Presented at the 39th Meeting of the Aeroballistic Range Association, Albuquerque, N. Mex., Oct. 1988.

5. Anderson, R.: Ballistics Research Laboratory, Aberdeen, Md. Personal communication, May 1995.

6. Hough, G.; and Liquornik, D.: Interior Ballistics Simulation of the UAH/ARC Light-GAS Guns. Presented at the 43rd Meeting of the Aeroballistic Range Association, Columbus, Ohio, Sept.–Oct. 1992.

7. Bernier, H.; and Gambart, J.: MOOREA, an Internal Ballistic Code for Two Stage Light Gas Gun Study. Presented at the 38th Meeting of the Aeroballistic Range Association, Tokyo, Japan, Oct. 1987.

8. Bernier, H.; and Gambart, J.: Le Code MOOREA: Interpretation du Fonctionnement d'un Canon a Gaz Leger. Presented at the 39th Meeting of the Aeroballistic Range Association, Albuquerque, N. Mex., Oct. 1988.

9. Glenn, L. A.: Performance Analysis of the Two-Stage Light Gas Gun. Presented at the APS Fifth Topical Conference on Shock Waves in Condensed Matter, Monterey, Calif., July 1987.

10. Bogdanoff, D. W.; and Brackett, D. C.: Godunov Computational Fluid Dynamics Method for Extreme Flow Velocities and Any Equation of State. AIAA J., vol. 27, July 1989, pp. 909–917.

11. Bogdanoff, D. W.; and Miller, R. J.: Improving the Performance of Two-Stage Gas Guns by Adding A Diaphragm in the Pump Tube. Presented at the 1994 Hypervelocity Impact Symposium, Santa Fe/Albuquerque, N. Mex., Oct. 1994.

12. Bogdanoff, D. W.; and Miller, R. J.: Optimization Study of the Ames 1.5" Two-Stage Light gas Gun. Submitted to the 34th Aerospace Sciences Meeting, Reno, Nev., Jan. 1996.

13. Seigel, A. E.: The Theory of High-Speed Guns. AGARDOgraph 91, May 1965, pp. 138–142.

14. Stull, D. R.; and Prophet, M. (project directors): JANNAF Thermochemical Tables. U. S. Government Printing Office, Washington, D.C., June 1970.

15. Zel'dovich, Y. B.; and Raizer, Y. P.: Physics of Shock Waves and High-Temperature Hydrodynamic Phenomena. Vol. II. Academic Press, N.Y., 1967, pp. 704, 705, and 710.

16. Marsh, S. P., ed.: LASL Shock Hugoniot Data. University of California Press, Berkeley, Calif., 1980.

17. Cooper, N. G., ed.: An Invitation to Participate in the LASL Equation of State Library. Report LASL-79-62, Los Alamos Scientific Laboratories, Los Alamos, N. Mex., 1979.

18. McAdams, W. H.: Heat Transmission. McGraw-Hill, N.Y., 1954, pp. 155–157.

19. Seigel, A. E.: The Theory of High Speed Guns. AGARDograph 91, May 1965, pp. 74–76.

20. van Driest, E. R.: Turbulent Boundary Layer in Compressible Fluids. J. Aero. Sci., vol. 18, Mar. 1953, pp. 145–160 and 216.

21. Shapiro, A. H.: The Dynamics and Thermodynamics of Compressible Fluid Flow. Ronald, N.Y., 1954, pp. 1100–1101.

22. Hinze, J. O.: Turbulence. 2nd ed., McGraw-Hill, N.Y., 1975, pp. 724–742.

23. Laufer, J.: The Structure of Fully Developed Pipe Flow. NACA TN 1174, 1954.

24. Schlichting, H.: Boundary-Layer Theory. 7th ed., McGraw-Hill, N.Y., 1979, pp. 598–612.

25. Bowden, F. P. and Tabor, D.: The Friction and Lubrication of Solids, Part II. Oxford University Press, Oxford, England, 1964, pp. 472–478.

26. Powell, E. S.; Winstead, C. A.; DeWitt, J. R.; and Cable, A. J.: A Preliminary Study of Wear in a Two-Stage Light-Gas Launcher. Presented at the 36th Meeting of the Aeroballistic Range Association, Southwest Research Institute, San Antonio, Tex., Oct. 1985.

27. Zowarka, R. C.; and Weldon, W. F.: Application of a Friction Model to Electromagnetic Launchers. Presented at the 37th Meeting of the Aeroballistic Range Association, Defence Research Establishment Valcartier, Courcelette, Quebec, Canada, Sept. 1986.

28. Powell, E. S.; DeWitt, J. R.; and Cable, A. J.: Further Study of Model Wear in a Two-Stage Light-Gas Launcher. Presented at the 37th Meeting of the Aeroballistic Range Association, Defense Research Establishment Valcartier, Courcelette, Quebec, Canada, Sept. 1986.

29. Groth, C. P. T.; Gottlieb, J. J.; and Bourget, C.: Ideal-Viscoplastic Extrusion Model with Application to Deforming Pistons in Light-Gas Guns. UTIAS Technical Note No. 266, University of Toronto Institute for Aerospace Sciences, Toronto, Ontario, Canada, Nov. 1987.

30. Peters, S. T.: Selected Properties of Navy Gun Propellants. Report IHSP 84-194, Naval Ordnance Station, Indian Head, MD, Feb. 1984.

31. MacCormack, R. W.: Current Status of Numerical Solutions of the Navier–Stokes Equations. AIAA Paper 85-0032, June 1985, p. 4.

32. Anderson, D. A.; Tannehill, J. C.; and Pletcher, R. H.: Computational Fluid Dynamics and Heat Transfer. McGraw-Hill, N.Y., 1984, pp. 482–484.

33. Addessio, F. L.; Carroll, D. E.; Dukowicz, J. K.; Harlow, F. H.; Johnson, J. N.; Kashiwa, B. A.; Maltrud, M. E.; and Ruppel, H. M.: CAVEAT: A Computer Code for Fluid Dynamics Problems with Large Distortion and Internal Slip. Los Alamos National Laboratory, Los Alamos, N. Mex., Report LA-10613-MS UC-32, Feb. 1986, pp. 119–137.

34. Wilson, G.: Time-Dependent Quasi-One-Dimensional of High Enthalpy Pulse Facilities. AIAA Paper 92-5096, Presented at the AIAA 4th International Aerospace Planes Conference, Orlando, Fla., Dec. 1992.

35. Bernier, H.: Flat-Scored High Pressure Diaphragms as Quick Opening Valves. Presented at the 42nd Aeroballistic Range Association Meeting, Adelaide, Australia, Oct. 1991.

36. Stiefel, L., ed.: Gun Propulsion Technology, Vol. 109, Progress in Astronautics and Aeronautics series. Published by the American Institute of Aeronautics and Astronautics, Washington, D.C., 1988, pp. 61–74.

37. Grollman, B. B.; and Nelson, C. W.: Burning Rates of Standard Army Propellants in Strand Burners and Closed Chamber Tests. Report BRL-MR-2775, U. S. Army Ballistics Research Laboratory, Aberdeen, Md., Aug. 1977.

38. Corner, J.: Theory of the Interior Ballistics of Guns. Wiley, N.Y., 1950, pp. 71–73.

39. Corner, J.: Theory of the Interior Ballistics of Guns. Wiley, N.Y., 1950, pp. 70–84.

40. Rast, J. J.: The Design of Flat-Scored High-Pressure Diaphragms for Use in Shock Tunnels and Gas Guns. NAVORD Report 6865, U. S. Naval Ordinance Laboratory, White Oak, Md., Jan. 1961.

41. Jones, N.: Structual Impact. Cambridge University Press, Cambridge, England, 1989, pp. 333–355.

42. Catalog, Commercial Plastics and Supply Corporation, 98-31 Jamaica Ave., Richmond Hill, N.Y., 1992, p. 131.

43. Zel'dovich, Y. B.; and Raizer, Y. P.: Physics of Shock Waves and High-Temperature Hydrodynamic Phenomena, Vol. II. Academic Press, N.Y., 1967, pp. 734, 735, 742, and 743.

44. Keener, E. R.; and Hopkins, E. J.: Use of Preston Tubes for Measuring Hypersonic Turbulent Skin Friction. Presented at the AIAA 4th Aerodynamic Testing Conference, Cincinnati, Ohio, Apr. 1969.

45. Golubev, I. F.: Viscosities of Gases and Gas Mixtures. Translated from Russian, Israel Program for Scientific Translations, Jerusalem, 1970, p. 62.

46. Hercules Medium Web Smokeless Powders. Data Sheets Obtained from Hercules Incorporated, Hercules Plaza, Wilmington, Del., 1990.

47. Golubev, I. F.: Viscosities of Gases and Gas Mixtures. Translated from Russian, Israel Program for Scientific Translations, Jerusalem, 1970, pp. 178–180.

48. Schlichting, H.: Boundary-Layer Theory. 7th ed., McGraw-Hill, N.Y., 1979, pp. 599–600.

REPORT DOCUMENTATION PAGE

Form Approved
OMB No. 0704-0188

1. AGENCY USE ONLY *(Leave blank)*	2. REPORT DATE	3. REPORT TYPE AND DATES COVERED
	September 1995	Technical Memorandum

4. TITLE AND SUBTITLE

New Higher-Order Godunov Code for Modelling Performance of Two-Stage Light Gas Guns

5. FUNDING NUMBERS

478-85-20

6. AUTHOR(S)

D. W. Bogdanoff and R. J. Miller

7. PERFORMING ORGANIZATION NAME(S) AND ADDRESS(ES)

Thermosciences Institute
Ames Research Center
Moffett Field, CA 94035-1000

8. PERFORMING ORGANIZATION REPORT NUMBER

A-950086

9. SPONSORING/MONITORING AGENCY NAME(S) AND ADDRESS(ES)

National Aeronautics and Space Administration
Washington, DC 20546-0001

10. SPONSORING/MONITORING AGENCY REPORT NUMBER

NASA TM-110363

11. SUPPLEMENTARY NOTES

Point of Contact: D. W. Bogdanoff, Ames Research Center, MS 230-2, Moffett Field, CA 94035-1000
(415) 604-6138

12a. DISTRIBUTION/AVAILABILITY STATEMENT

Unclassified-Unlimited
Subject Category – 64

Available from the NASA Center for AeroSpace Information,
800 Elkridge Landing Road, Linthicum Heights, MD 21090; (301) 621-0390

12b. DISTRIBUTION CODE

13. ABSTRACT ***(Maximum 200 words)***

A new quasi-one-dimensional Godunov code for modelling two-stage light gas guns is described. The code is third-order accurate in space and second-order accurate in time. A very accurate Riemann solver is used. Friction and heat transfer to the tube wall for gases and dense media are modelled and a simple nonequilibrium turbulence model is used for gas flows. The code also models gunpowder burn in the first-stage breech. Realistic equations of state (EOS) are used for all media. The code was validated against exact solutions of Riemann's shock-tube problem, impact of dense media slabs at velocities up to 20 km/sec, flow through a supersonic convergent-divergent nozzle and burning of gunpowder in a closed bomb. Excellent validation results were obtained. The code was then used to predict the performance of two light gas guns (1.5 in. and 0.28 in.) in service at the Ames Research Center. The code predictions were compared with measured pressure histories in the powder chamber and pump tube and with measured piston and projectile velocities. Very good agreement between computational fluid dynamics (CFD) predictions and measurements was obtained. Actual powder-burn rates in the gun were found to be considerably higher (60–90 percent) than predicted by the manufacturer and the behavior of the piston upon yielding appears to differ greatly from that suggested by low-strain rate tests.

14. SUBJECT TERMS

Godunov code, Two-stage light gas guns, High pressure equations of state

15. NUMBER OF PAGES

46

16. PRICE CODE

A03

17. SECURITY CLASSIFICATION OF REPORT	18. SECURITY CLASSIFICATION OF THIS PAGE	19. SECURITY CLASSIFICATION OF ABSTRACT	20. LIMITATION OF ABSTRACT
Unclassified	Unclassified		